Geophysical Journal International

Geophys. J. Int. (2026) **246,** 1–22
Advance Access publication 2026 February 27
Research Paper

https://doi.org/10.1093/gji/ggag083

Assessing the impact of automatically derived depth phases on the determination of earthquake hypocentres—application to the South American subduction zone

Alice Blackwell [1], Timothy Craig,[2] Sebastian Rost [1], Thomas Garth[3] and Ryan Gallacher[3]

[1]*Institute for Geophysics and Tectonics, University of Leeds, Leeds, LS2 9JT, UK*
[2]*COMET, Institute for Geophysics and Tectonics, University of Leeds, Leeds, LS2 9JT, UK. E-mail: t.j.craig@leeds.ac.uk*
[3]*International Seismological Centre, Pipers Lane, Thatcham, Berkshire RG*194*NS, UK*

Accepted 2026 February 23. Received 2026 January 22; in original form 2025 October 13

SUMMARY

Accurate earthquake hypocentres are fundamental to a wide range of geophysical studies, yet source depth remains poorly constrained in teleseismic earthquake catalogues. Near source surface reflections such as *pP*, *sP* and *sS* (known as depth phases) provide critical information for resolving hypocentral depth, particularly for intermediate-depth earthquakes. The number of depth phases reported by global earthquake monitoring agencies has declined significantly in recent decades, potentially reducing the precision of resolved earthquake depths. To address this, we automatically detect *P*, *pP*, *sP*, *S* and *sS* phase arrivals using teleseismic *ad-hoc* arrays. We detect these phases for earthquakes in the South American Subduction Zone (SASZ) at depths of 40–350 km and between m_b 4.7 to 6.5. The identified phases are integrated with the phases reported to the ISC Bulletin, and used to relocate earthquakes with ISCloc. We assess the impact of incorporating automatically detected, *ad-hoc* array-derived depth phases on earthquake relocations across the SASZ, and find an improvement in depth resolution for 88.8 per cent of earthquakes. Using this enhanced catalogue we investigate the structure of the Wadati–Benioff zone, focusing on two significant earthquakes: the 2005 M_w 7.7 Tarapacá and 2019 M_w 8.0 Peru events. Finally, we successfully apply our methodology to deep focus earthquakes (350–700 km), which further define the deepest portion of the seismogenic slab. Our results demonstrate the potential for automatically detected, *ad-hoc* array-derived depth phases to substantially improve the accuracy of teleseismic earthquake hypocentres, and offer further constraint upon slab geometry and seismogenic structure.

Key words: earthquake monitoring and test-ban treaty verification; earthquake parametrization; Earthquake source observations.

1 INTRODUCTION

The accurate location of earthquakes using globally distributed seismic data underpins a wide range of solid-Earth geophysics, from seismic hazards assessment to nuclear security, regional tectonics to global-scale tomographic imaging. The depth of an earthquake is generally the least well determined dimension of an earthquake hypocentre, particularly when locating an earthquake using teleseismic (i.e. seismic phases recorded 30°–90° from the source) phases. This can be mitigated by using near-source surface reflections arriving at a station shortly after their related direct arrival (e.g. *pP* and *sP* in the coda of *P*, *sS* in the coda of *S*), known as depth phases. This is effective due to the relative delay times between a direct arrival and the depth phases, which provide crucial constraints on the source depth of an earthquake, and are largely independent of the lateral location or origin time.

Whilst the identification of distinct depth phases is difficult for earthquakes at shallow depth due to overlap and interference with the direct phase, for earthquakes deeper than ∼25 km the incorporation of a significant number of depth phases can result in high-precision depths and therefore improved hypocentre resolution. This is further complemented by the vast data coverage offered by routinely operating seismic stations around the

world, which opens up the potential to expand high-precision earthquake relocation to unprecedented regions and scales. The increasing coverage of seismic data combined with the detection and application of depth phases can help to enhance our understanding of the intermediate-depth and deep focus seismicity, typically associated with subduction, and therefore the evolution of subducted slabs as they descend into the mantle.

In the last two decades the number of depth phases reported from global seismic monitoring agencies to the International Seismological Centre (ISC), which is responsible for collecting and preparing the definitive summary of world seismicity, has substantially decreased. This is likely due to the technical difficulty of picking depth phases coupled with limited picking resources at data centres. Consequently, the number of depth phases used in ISC relocations has dropped from ∼8000–17 000 to ∼4000–7000 per month (Fig. 1). The difficulties associated with depth phase picking also mean that not all depth phase readings are reliable, and the reduction in reported depth phases potentially increases the impact of erroneously reported depth phases. Without the incorporation of reliable depth phases (typically from two or more independent sources), teleseismic hypocentres of relatively deep earthquakes ($\geq$25 km) will have reduced depth resolution, leading to increased uncertainty in the other location parameters (lateral location and origin time). Therefore, there has been increased motivation to pick depth phases, either manually or automatically, to backfill the lack of reported depth phases and improve their earthquake relocations.

A. Blackwell *et al.* (2024) developed a new approach building on the work of M. Florez & G. Prieto (2017) to leverage the growing density of routinely operating seismic stations, where the waveforms are openly accessible. This approach relies on assembling and processing *ad-hoc* arrays to increase the signal-to-noise ratio of the phases (J. Ward *et al.* 2023), and automatically picking the beams derived from these *ad-hoc* arrays for *P*, *pP* and *sP* arrivals expressly to improve depth determination in Peru and northern Chile. The approach of A. Blackwell *et al.* (2024) does not account for 3-D variations in earthquake location and depth, nor does it incorporate depth phase bounce point corrections when determining earthquake depth. These are significant assumptions to apply to regions in South America, given the local Andean mountain range and associated crustal geometries (T. Craig 2019), as is the assumption (common in teleseismic studies) that lateral location is unchanged when re-determining hypocentre depth. We can account for these assumptions by integrating the increased observational data available, using the approach outlined in A. Blackwell *et al.* (2024), with a more comprehensive location procedure, such as the ISC relocation algorithm, ISCloc (I. Bondár & D. Storchak 2011). ISCloc calculates the earthquakes latitude, longitude, origin time and depth as well as determining the uncertainty in these parameters through an iterative linearized inversion. Traveltimes are calculated using the ak135 1-D global velocity model (B. Kennett *et al.* 1995) and depth phase bounce point corrections are calculated from a 0.5 degree resolution topography (E. Engdahl *et al.* 1998; I. Bondár & D. Storchak 2011).

In this paper, we test the impact of adding automatically derived depth phases to the wider set of seismic phases reported in the ISC Bulletin, using an expansive data set encompassing the South American Subduction Zone (SASZ) and the ISCloc location algorithm. We show an improvement in the depth resolution of both the previous catalogue reported by A. Blackwell *et al.* (2024) and the ISC Bulletin in the region, demonstrating the benefits of augmenting a phase catalogue with *ad-hoc* array determined depth phases. Furthermore, we also investigate the impact of the newly relocated earthquakes upon the current understanding of the Wadati–Benioff zone (K. Wadati 1935; H. Benioff 1949) in northern Chile, the 2005 M_w 7.7 Tarapacá and 2019 M_w 8.0 Peruvian earthquakes. As part of this work, we extend the approach of A. Blackwell *et al.* (2024) to accommodate transverse-component *ad-hoc* array data for the detection of the direct *S* wave and its principal depth phase, *sS*, and further apply this method to relocate deeper earthquakes.

1.1 South American Subduction Zone (SASZ)

At the SASZ margin the Nazca and South American plates converge, as the Nazca plate subducts eastwards beneath South America. The margin extends from approximately 6°S to 45°S in latitude, with the plates converging at ∼5.6–6 cm yr^{-1} in the direction of ∼81–83°N (R. Trenkamp *et al.* 2002). This encourages increasingly oblique convergence north of Chile, where the subduction trench curves westward (E. Rodríguez *et al.* 2024). The downgoing Nazca plate in the SASZ has a number of bathymetric features (Fig. 2) which are thought to influence seismicity and slab geometry in the region, such as fracture zones and ridges (N. Espurt *et al.* 2008; S. Bilek 2010; Y. Gao *et al.* 2021), and two named flat slab sections – the Peruvian and Pampean flat slabs (N. Flament *et al.* 2015). The margin also has associated arc volcanism; the locations of the Holocene volcanoes are illustrated in Fig.2 By extending the approach of A. Blackwell *et al.* (2024) to include the entire SASZ, and incorporating new phases (*S* and *sS*), we aim to generate catalogues which can be used to assess further links between seismicity and the background geodynamic setting. In the later stages of this work, we consider the implications of the revised seismicity catalogue on our understanding of the geometry and dynamics of the Wadati–Benioff zone and subducted plate, as well as for understanding the seismic activity in areas which hosted large-magnitude intraslab earthquakes (the 2005 Tarapacá and 2019 northern Peru earthquakes).

2 EARTHQUAKE RELOCATION WITH ISCLOC

We build upon and apply the methodology documented in A. Blackwell *et al.* (2024), to determine arrival times for teleseismic *P*, *pP*, *sP*, *S* and *sS* phases from array processed data. This aims to boost the signal-to-noise ratios of typically very small amplitude arrivals, relative to what is possible with a single seismic station. The arrays are assembled for each earthquake from the available teleseismic stations using unsupervised machine learning and are used for phase detection (further detail can be found in Section 2.3). We then combined these *ad-hoc* array determined arrivals with previously reported phase arrivals (archived at the ISC) and use the combined data set to relocate earthquakes using ISCloc (I. Bondár & D. Storchak 2011) (which solves for earthquake latitude, longitude, depth and origin time). We begin with an initial earthquake hypocentre catalogue for the SASZ—the selection of which is described in Section 2.1—which we aim to refine by increasing the number of depth phases available for hypocentre determination. We will demonstrate the methodology with an example earthquake (m_b 6.0 from 2016 July 25, located in Chile) to illustrate the *ad-hoc* array processing and analysis steps.

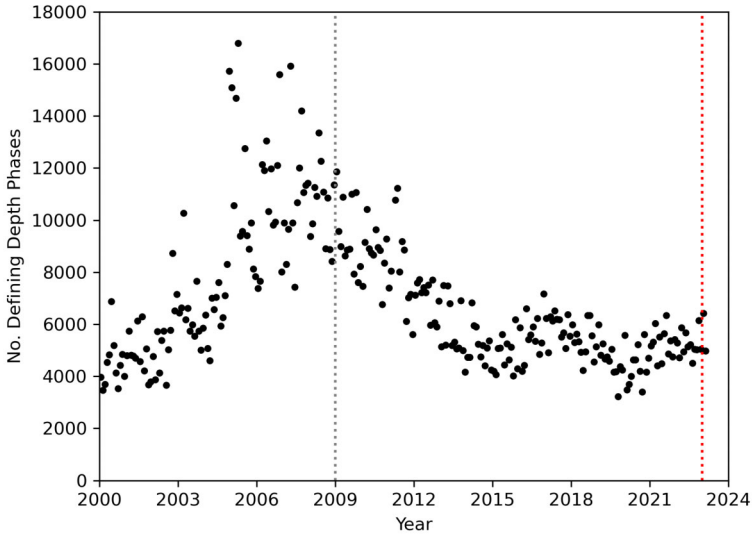

Figure 1. Number of depth phases (*pP*, *sP*, *pwP*, *sS* and surface reflected core phases) defining ISC earthquake hypocentres against the year the earthquake occurred (ISC, personal comms.). Grey dotted line highlights the beginning of 2009, where numbers begin to decline. Red dotted line shows the beginning of 2023, where the reviewed ISC catalogue approximately ends at time of writing.

2.1 Initial catalogue

The approach we have developed looks to refine intermediate-depth earthquake hypocentres which have already been determined by an external agency. For our initial SASZ earthquake catalogue, we take all earthquakes recorded in the ISC catalogue along the South American Subduction Zone from 1995 January 1 to 2024 September 9, with depths of 40–350 km. In keeping with the conclusions of A. Blackwell *et al.* (2024), we do not consider earthquakes shallower than 40 km, as the direct and depth phases are likely to overlap, and we limit the magnitudes for which we attempt relocation to m_b 4.7–6.5. We find 2877 events within these search criteria (Fig. 2), which are the events that are considered for our relocation approach outlined below.

2.2 Data processing

For each earthquake in the initial catalogue taken from the ISC (see Section 2.1), all available BH∗ or HH∗ channel teleseismic data (recorded between 30° and 90° epicentral distance), and their metadata, are downloaded from open access FDSN servers using ObspyDMT (K. Hosseini & K. Sigloch 2017). These data are then pre-processed to prepare for the array-based approach discussed in Section 2.3.

We discard traces with gaps or missing data, and rotate horizontal components into the N and E orientations (if they are not already), using the component orientation stored in the metadata. The instrument responses are then deconvolved from the waveforms, and waveform data are converted to velocity, linearly de-trended, demeaned, have a 5 per cent end taper applied, bandpass filtered, are resampled to 10 Hz and are normalized to their peak absolute amplitude. Data for Z-component and 3-component data are processed differently since they are used for the analysis of *P* wave (and depth phases) and *S*-wave (and depth phases), respectively. The different approaches are shown in the two processing boxes in Fig.3 The bandpass filter applied also depends on the component. Z-component data are filtered between 0.1 and 1.0 Hz, whilst horizontal component data are filtered between 0.03 and 0.2 Hz. For the duration of the seismic data processing, the Z components and horizontal components are handled independently, with horizontal components for a station only being processed if the station has 3-component data. Fig. 3 summarizes the data processing workflow.

2.3 Detecting *P*, *pP*, *sP*, *S* and *sS* picks using adaptive *ad-hoc* arrays

To determine the *P*, *pP*, *sP*, *S* and *sS* phases, used to refine the earthquake hypocentres (see Section 2.5), array processing is applied to boost the phase signal-to-noise ratios for automatic picking. A summary workflow of the array processing steps and phase identification is shown in Fig.4

2.3.1 Creating ad-hoc arrays

For an earthquake with pre-processed Z-component seismic data, stations are grouped into *ad-hoc* arrays using a combination of DBSCAN clustering (M. Ester *et al.* 1996) and Ball-Tree nearest neighbour algorithms (F. Pedregosa *et al.* 2011; J. Ward *et al.* 2023; A. Blackwell *et al.* 2024). The DBSCAN algorithm searches for sufficiently dense station distributions to form arrays with at least 10 stations within a 2.5° aperture, and identifies a central core station per array. Array aperture is determined by the longest wavelength of interest which determines the minimum size of the array at which it operates and is frequency dependent (here 0.1 to 1 Hz for *P* waves and 0.03 to 0.2 Hz for *S* waves) (S. Rost & C. Thomas 2002; A. Blackwell *et al.* 2024). The nearest neighbour algorithm selects the stations within the aperture of each core station to generate *ad-hoc* arrays. For the example earthquake, which occurred on 25th July 2016 in Chile at (26.1551°S, 70.4548°W), there are 1789 stations with processed Z-component data, which are clustered into 88 *ad-hoc* arrays containing 1229 of the available stations (Fig. 5). Therefore, there are 560 stations with Z-component data which were not incorporated into an *ad-hoc* array—these stations are located too sparsely to generate an array which fits the density parameter.

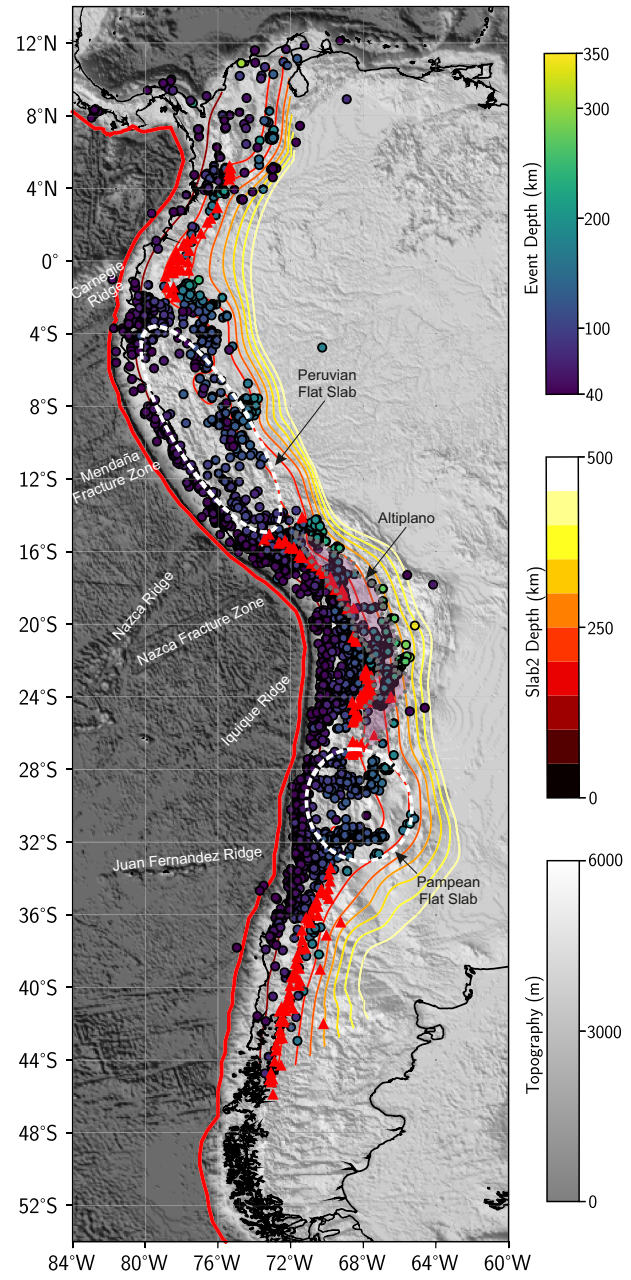

Figure 2. Map of the initial earthquake catalogue (circles) used for the SASZ intermediate-depth earthquake relocation. The thick red line shows the location of the subduction trench, and red triangles represent the locations of Holocene volcanoes (Global Volcanism Program 2024). Other bathymetric and slab features are labelled (G. Zandt *et al.* 1994; N. Espurt *et al.* 2008; S. Bilek 2010; N. Flament *et al.* 2015).

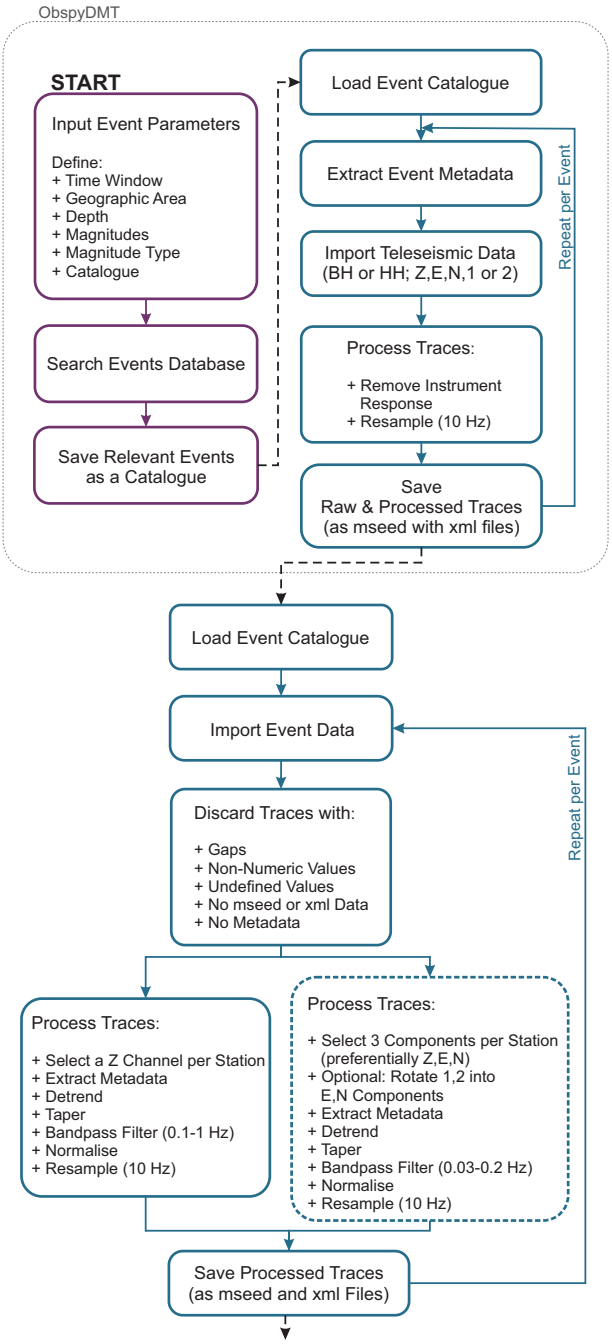

Figure 3. Summary workflow for processing 3-component teleseismic data for array processing in Section 2.3.

To process *P* coda arrivals (hereby referring to *P*, *pP* and *sP*) the Z-component seismic data are arranged into *ad-hoc* arrays. For targeting *S* coda arrivals (hereby referring to *S* and *sS*, *S* coda processing is optional throughout this workflow), the available 3-component stations are assembled into the same *ad-hoc* arrays defined for *P* coda arrivals. Typically there are fewer stations available within an *ad-hoc* array which have data available for all 3 components, this can cause a number of 3-component *ad-hoc* arrays to have less than the required 10 stations or no stations at all. For the SASZ, 285 213 *ad-hoc* arrays are generated for the entire initial catalogue using Z-component data, and only 89 024 *ad-hoc* arrays with 10 or more stations are re-created using 3-component data (31.2 per cent). For the example earthquake from 2016 July 25, there are 88 *ad-hoc* arrays created from the Z-component data, with only 72 from the 3-component data. Despite the reduction in *ad-hoc* array quantity, designing the *S* coda workflow to be dependent upon the *P* coda workflow significantly simplifies the approach.

As Fig. 5 demonstrates, array-construction at teleseismic distances for South America is heavily dominated by the density of instruments available in North America, Europe (for events in the northern half of the SASZ) and Central America (for events in the southern two-thirds of the SASZ), supplemented by sparse

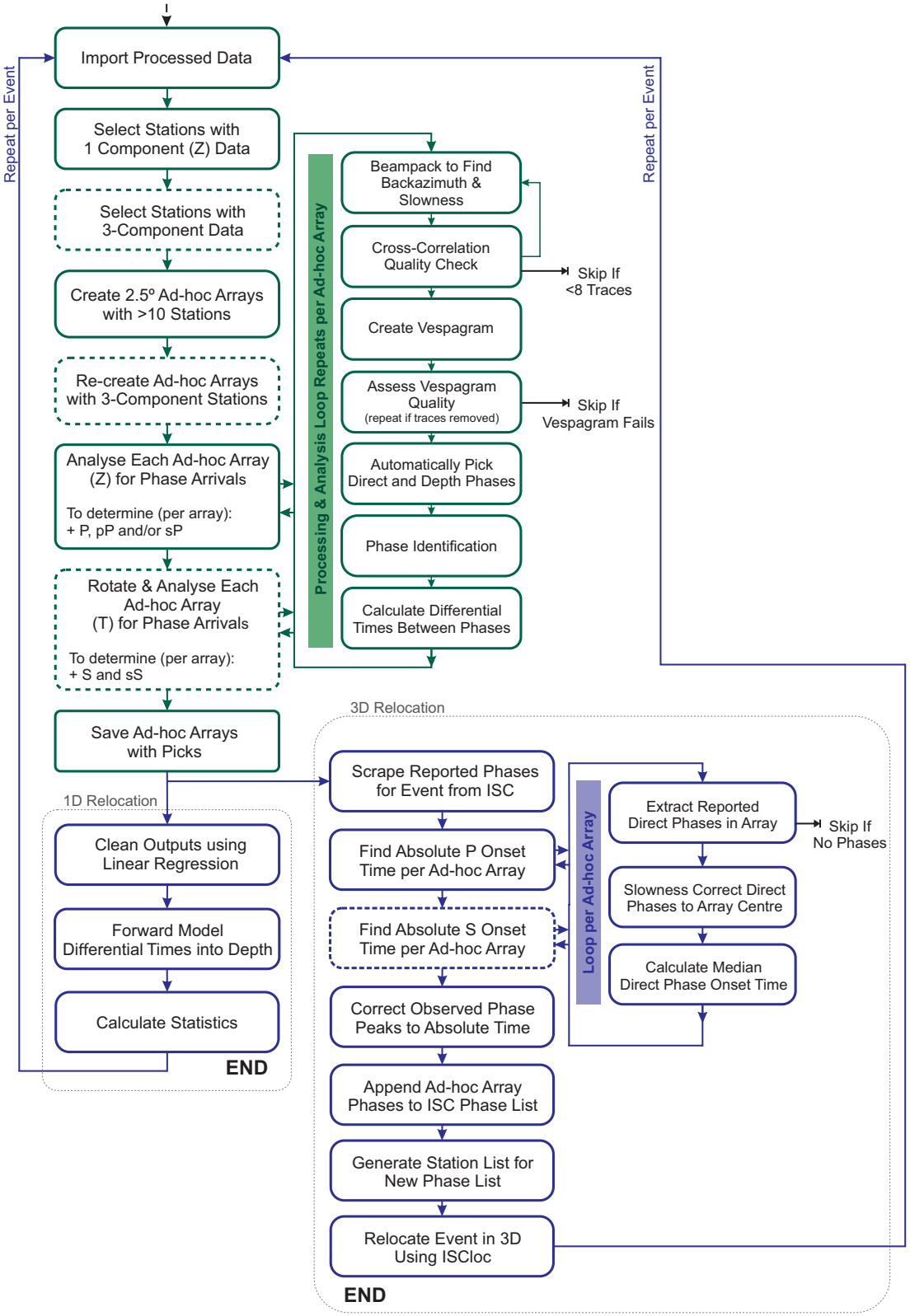

Figure 4. Summary workflow for relocating an earthquake using array processing described in Section 2.3, 2.4 and 2.5, including 1-D relocation discussed in A. Blackwell *et al.* (2024). Dashed boxes indicate steps associated with *S* coda arrivals.

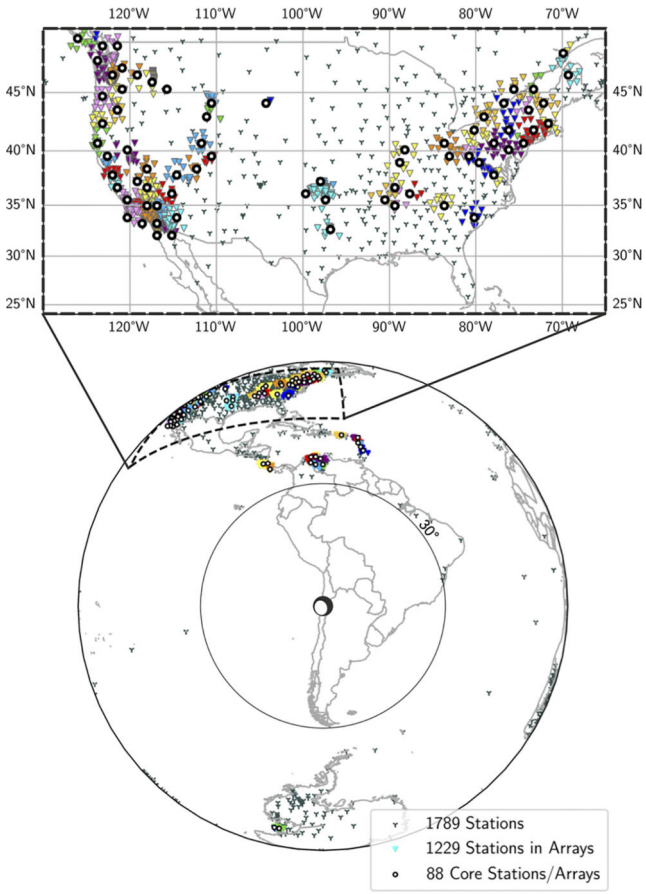

Figure 5. Example of the *ad-hoc* array creation process for a m_b 6.0 earthquake from 2016 July 25 located in Chile, showing a global distribution of teleseismic stations with processed Z components and the subsequent *ad-hoc* arrays (bottom), and a zoom in of the *ad-hoc* arrays created in the USA (top). The core stations per *ad-hoc* array are shown as thick black circles and the associated *ad-hoc* array stations as coloured triangles. The unused stations (grey Ys) are those removed via the DBSCAN routine, prior to the Ball-Tree process. The earthquake focal mechanism is taken from the Global Centroid Moment Tensor Project (GCMT) (A. Dziewonski *et al.* 1981; G. Ekström *et al.* 2012).

arrays in Antarctica, Africa and New Zealand. This leads to a relatively narrow azimuthal distribution of *ad-hoc* arrays. Whilst the dominance of northern azimuths for the SASZ is clear, the uneven distribution of global instrumentation at the required densities (typically limited to continental regions, and for Open Access data, dominated by North America, Europe, Oceania and East Asia) remains true for most regions of active seismicity.

2.3.2 *Determining best-fitting backazimuth and slowness*

After the *ad-hoc* arrays have been established, our approach can take advantage of array processing to boost the signal-to-noise ratios of the small-amplitude depth phases *pP*, *sP* and *sS*). For both the Z-only and 3-component versions of each *ad-hoc* array, the best-fitting backazimuth and slowness for the *P* and *S* waves are found directly from the station data by beampacking the arrivals (A. Blackwell *et al.* 2024). The Z-component *ad-hoc* array data are trimmed around the ak135 (B. Kennett *et al.* 1995) modelled *P* arrival, and beamformed with a range of test slownesses (± 0.04 s km^{-1} in intervals of 0.001 s km^{-1}) and backazimuths ($\pm 15^\circ$ in 1° intervals) centred on the ray-theoretical values from using ray tracing (H. Crotwell *et al.* 1999). The backazimuth and slowness which result in the largest amplitude beam are selected as the best-fitting slowness vector values. The best-fitting slowness/backazimuth from the main phases (*P*/*S*) are used to form the beam for further analysis. We find that the depth phases show similar slowness/backazimuth deviations to the main phases (Fig. 8). The small slowness difference between main phase and depth phase are within the slowness resolution of the *ad-hoc* arrays.

For a 3-component *ad-hoc* array, the best-fitting backazimuth found from the Z-component data is used to rotate the horizontal components into radial and transverse orientations. If the Z-component *ad-hoc* array fails to provide a beampack determined backazimuth, the theoretical backazimuth based on the initial catalogue hypocentre is used instead. Given that the approach intends to pick *S* and *sS*, the transverse (T) component is taken forward for further analysis. The best-fitting slowness and backazimuth are searched for using the same beampacking approach applied to the Z-component data. However this time the T-component data is trimmed to include the ak135 (B. Kennett *et al.* 1995) modelled *S* arrival, and the test ranges straddle the expected *S* wave slowness and backazimuth.

Fig. 6 shows examples of the beampacking parameter search to extract the best-fitting slowness and backazimuth values for both *P* and *S* waves (filled red circles on a and d), and their resultant beams (c and f), for the same *ad-hoc* array. A comparison to the expected values is additionally provided (hollow red circle on a and d), and the beams they construct (b and e). We find that using slowness/backazimuth values measured through the array processing improve the quality, especially the signal-to-noise ratio and waveform geometry of the array stacked beam over those generated using the ray-theoretical values based on source–receiver combination and a 1-D velocity model. The slowness vector (or slowness/backazimuth) differences are likely due to near-receiver velocity structure. The improved beam suppresses incoherent noise more effectively and improves our ability to automatically pick the main- and depth-phases from the improved beams.

2.3.3 *Data quality control*

We apply two data quality tests to ensure that only *ad-hoc* arrays with clear, coherent arrivals are considered for automatic picking. Our automatic picking routine (Section 2.3.4) relies upon fourth order phase weighted beams (M. Schimmel & H. Paulssen 1997) for phase detection, we therefore also use phase weighted beams during our quality control tests to ensure continuity between the two processes.

We first compare each trace in the *ad-hoc* array to the resultant optimum, phase weighted beam (created with the beampack determined slowness and backazimuth) using cross-correlation. Any trace which has a cross-correlation coefficient less than 0.3 or which requires a time-shift greater than 0.5 s to align the trace to the beam, is discarded (A. Blackwell *et al.* 2024). If the *ad-hoc* array has less than eight traces after this test, the *ad-hoc* array is removed from further analysis. If the *ad-hoc* array has eight traces or more, the *ad-hoc* array analysis begins again, to redetermine the best-fitting slowness and backazimuth from the remaining traces, using the beampacking routine.

Secondly, we assess the coherency of the arrivals in the *ad-hoc* array data by considering their slowness vespagram. Fourth order phase weighted vespagram beams are constructed using

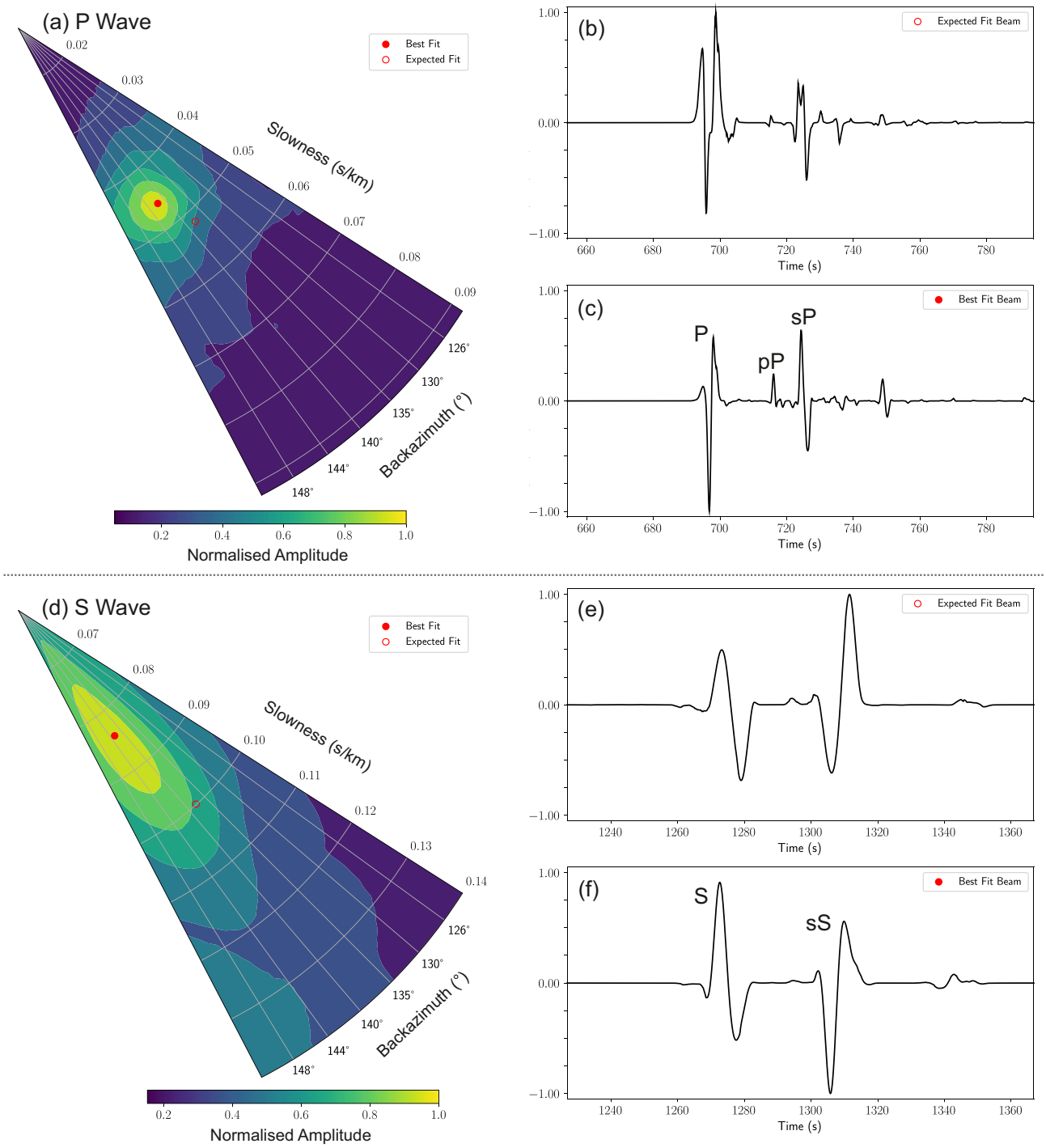

Figure 6. *P*- and *S*-wave amplitudes during beamforming in polar coordinates (backazimuth and slowness) to determine the best-fitting backazimuth and slowness parameters directly from the *ad-hoc* array traces (a and d). The open red circle shows the expected slowness and backazimuth found through ray tracing and the corresponding phase-weighted beam in (b) and (e). The filled red circle shows the beampack derived values and the resultant phase-weighted beam in (c) and (f), showing the importance of using measured backazimuth and slowness values. Example from m_b 6.0 earthquake from 2016 July 25, *ad-hoc* array at 75.1° epicentral distance.

the same test slowness range used during the beampacking routine, and the beampack-determined backazimuth. On the resultant normalized vespagram, any peaks greater than 0.6 of the largest amplitude peak are selected, categorized into clusters using DBSCAN (M. Ester *et al.* 1996), and the cluster centres are extracted. These cluster centres are expected to represent the *P* or *S* coda arrivals for the Z and T-component *ad-hoc* arrays, respectively, and therefore, are expected to align along the beampack-determined slowness. If the clusters are prominent at an unexpected slowness on the vespagram, that is an indication that the

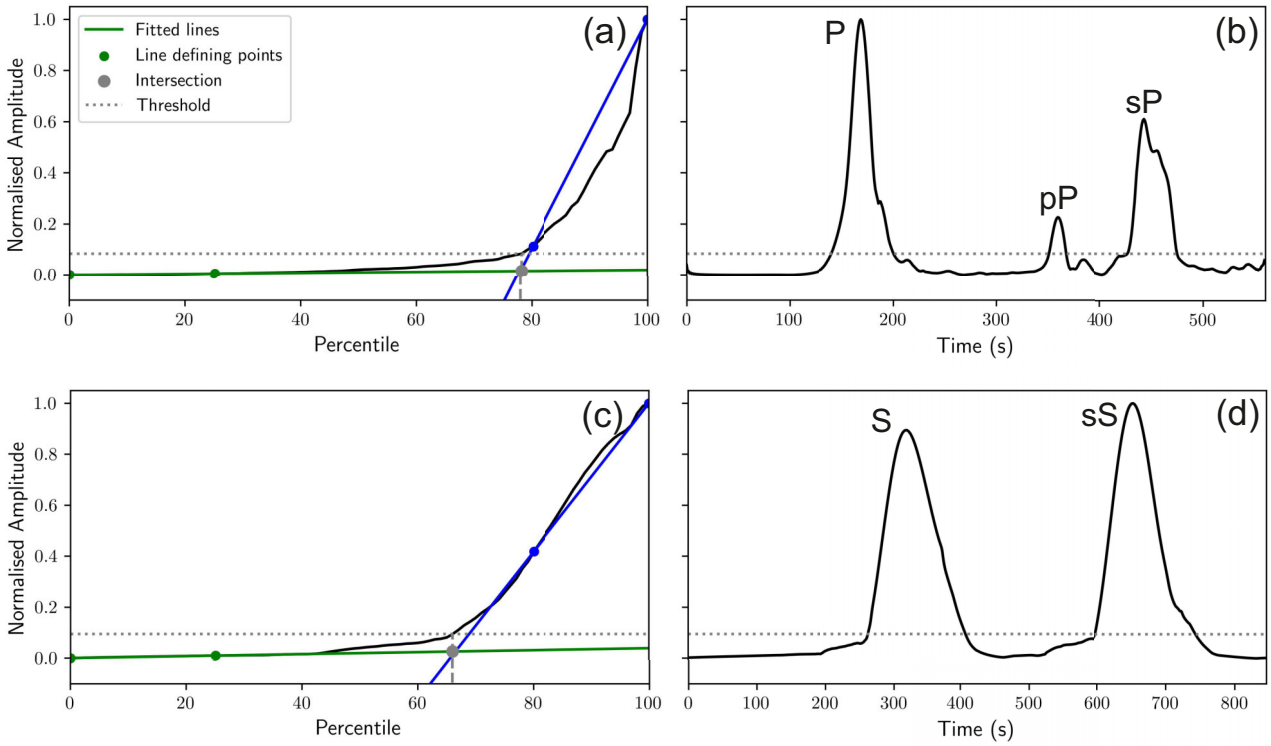

Figure 7. Example of the automatic picking threshold found for an *ad-hoc* array at an epicentral distance of 75.1° from the m_b 6.0 earthquake on 2016 July 25. Distribution of amplitude values for the *ad-hoc* array beam with respect to the percentile, the approximation of the beam with two lines, their intersection and the final threshold found for the Z (a) and T (c) components. Threshold relative to the envelope of the phase-weighted beam for the Z (b) and T (d) components.

ad-hoc array is too complex or poor quality to automatically pick. A set of criteria from A. Blackwell *et al.* (2024) are used to identify poor quality vespagrams. Specifically if the mean slowness is within 0.006 s km^{-1} of the expected beampack-determined slowness and the standard deviation of the cluster centres is $<$0.0105 s km^{-1}, then the *ad-hoc* array passes the quality threshold. If these criteria are failed on either grounds, the *ad-hoc* array is discarded. Examples of different quality vespagrams are shown in Supplementary Fig. S1.

These quality control tests are separately applied to the Z and T-component *ad-hoc* arrays for a given earthquake. However, for the T-component *ad-hoc* array to be processed and analysed, the equivalent Z-component *ad-hoc* array must have passed the quality standards set. Furthermore, since the T-component *ad-hoc* arrays are arranged suboptimally to match those created with the Z-component data, and often have a reduced number of traces per *ad-hoc* array (hence a 68.8 per cent reduction in *ad-hoc* arrays with more than 10 stations), the T-component *ad-hoc* arrays are more likely to be discarded by the quality control tests.

2.3.4 Automatic phase detection and identification

After the quality control routines have been applied, the *ad-hoc* array is eligible to be automatically picked using a threshold-based approach. We detect phases using the envelope of the normalized optimum, phase weighted beam. To pick the arrival times of the main and depth phases we apply the threshold approach by A. Blackwell *et al.* (2024). Onsets are characterized by rapid amplitude increases of the coherent phases. We find the onset of the arrival from the onset of the amplitude increase by approximating the pre- and post-increase linear slopes and determining their intersect. Comparison with manual picking shows good correlation between the two methods. Other approaches have been tested (A. Blackwell *et al.* 2024). The dynamic threshold for a given *ad-hoc* array beam is determined from the distribution of amplitudes in the envelope by approximating the percentile (and thus, amplitude) after which larger amplitudes represent significant signal (Fig. 7). Peaks which exist above this dynamic threshold, and have a prominence greater than 0.15 of the maximum peak found in the beam are selected as candidates for our phases. For phase detection the beam for the *ad-hoc* array is trimmed to only include the expected phases, using arrival times determined through the ak135 1-D Earth model (B. Kennett *et al.* 1995) (e.g. 98 per cent of the modelled *P* arrival time to 102 per cent of the modelled *sP* arrival, for picking the *P* coda).

These candidates are subsequently passed to a phase detection routine to determine the most likely depth phases. For the *P* wave and its coda, we use a selection routine designed to identify one, two or three peaks (for *P*, *pP* and *sP*) from the Z-component data, based on maximizing the likelihood that a set of peaks represents a coherent set of relative phase times (we outline this approach in detail in A. Blackwell *et al.* 2024). For the more simple case of *S* and its coda, as we are working with T-component data, we avoid any ambiguity in the identity of a depth phase detected, as there is only one depth phase (*sS*). We therefore identify the most likely pair of peaks for *S* and *sS* based on comparison with relative arrival times for ak135 modelled arrivals (B. Kennett *et al.* 1995). The best-fitting sets of *P* and *S* coda peaks are selected as the final phase picks (note that *P* and *S* candidate peaks are independently assessed, Fig. 8), however if multiple

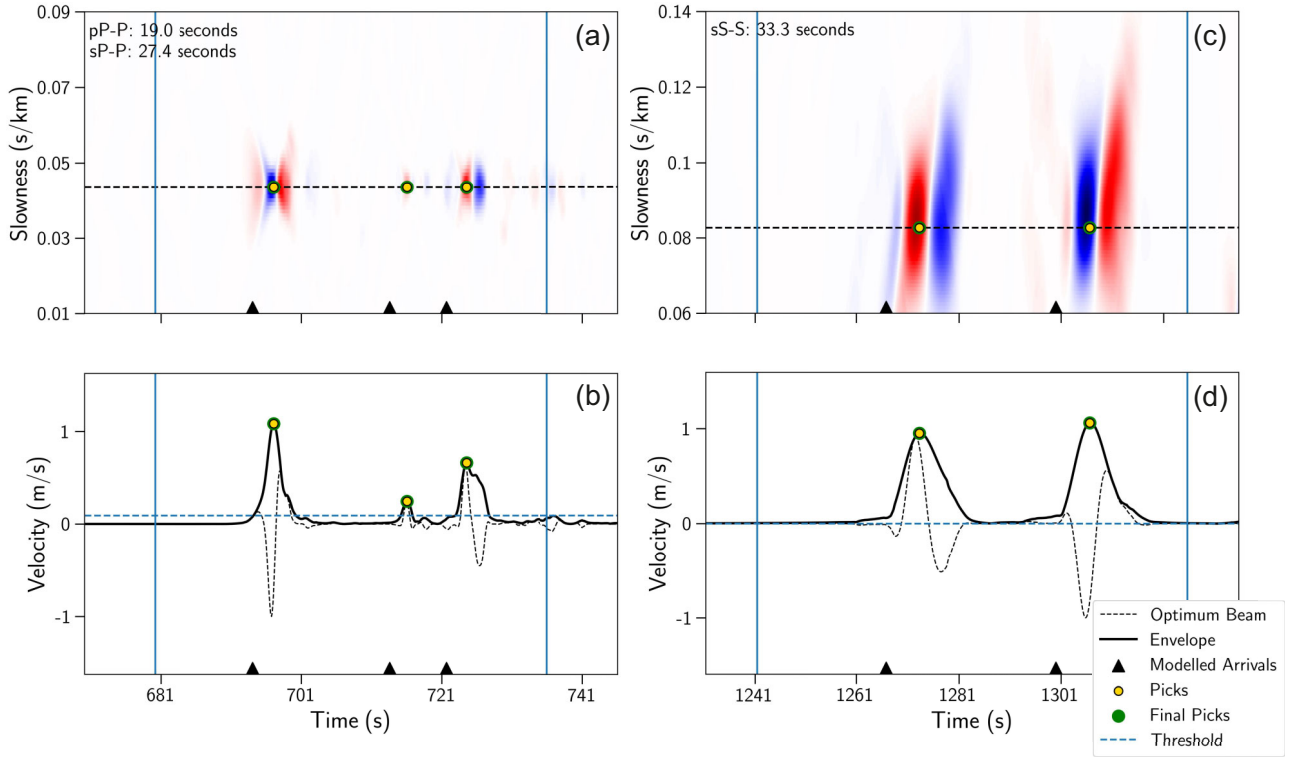

Figure 8. Example Z and T-component *ad-hoc* arrays located 75.1° from the earthquake, their automatic picks and differential times between phases for the m_b 6.0 earthquake which occurred on 2016 July 25 in Chile. (a) and (b) are the vespagram and optimum beam respectively for the Z-component *ad-hoc* array, whilst (c) and d) are the vespagram and beam for the T-component *ad-hoc* array. Blue vertical lines indicate the time window of data used for automatic picking.

trios or pairs of phases are appropriate for the phases, the largest combined amplitude sets are selected. Equally if a suitable trio of *P*, *pP* and *sP* picks is not found, pairs of *P* and *pP* or *P* and *sP* are searched for instead. If there are no pairs found from the Z or T-component data candidate picks, no phases are detected.

Each *ad-hoc* array for a given earthquake is analysed as described in this section (Section 2.3), with each Z-component *ad-hoc* array processed and analysed before the equivalent T-component data. Fig. 9 illustrates the success rate for the 2016 July 25 earthquake, by showing which *ad-hoc* arrays produced phase picks for both the Z and T-component data. The Z-component data generated 88 *ad-hoc* arrays, resulting in 73 picked *ad-hoc* arrays (this could be *P* and either *pP* or *sP*, or all 3 phases). Whilst the T-component data provided 72 *ad-hoc* arrays, using the previously defined Z-component *ad-hoc* arrays, and 57 of those provided picks (both *S* and *sS*). The T-component workflow suffers from a greater loss of data, due to the current requirement to construct the same *ad-hoc* arrays used for the Z-component data, and link their processing to the success of the equivalent Z-component *ad-hoc* array.

2.4 Converting amplitude picks to onset times

Previously A. Blackwell *et al.* (2024) used the relative timing of *P*-wave coda arrivals determined from the *ad-hoc* arrays to directly determine earthquake depth. The picking approach employed is designed to select the amplitude maxima of the phases, as opposed to the phase onsets. This improves the ability to automatically and consistently pick phases, and proved sufficient for using the relative arrival times of the phases to determine earthquake depth. However, integrating the *ad-hoc* array-observed phases with phases reported by the ISC Bulletin, in preparation for relocation with ISCloc, requires us to correct the amplitude picks to absolute onset arrival times, rather than using relative arrival times.

For simplicity, we use *P*-wave arrivals reported to the ISC to inform our required time-shift. We therefore developed an approach to extract the stations with time-defining (hypocentre defining) *P* phases reported for a given earthquake from the ISC Bulletin. We associate the stations with the *ad-hoc* arrays, slowness correct the phases to the geometric centre of the *ad-hoc* arrays and calculate the median *P* onset time (when there are multiple) for a given *ad-hoc* array. The difference between the ISC catalogue derived *P* arrival time and the *P* amplitude pick from the *ad-hoc* array data is determined and used as the time-shift correction for the *pP* and *sP* phases. The ISC catalogue derived *P* arrival is used as the corrected *P* onset time.

This approach means that if there is not a *P* arrival reported by a station within an *ad-hoc* array, that *ad-hoc* array's picks cannot be corrected and thus used. This is a common occurrence for earthquakes after 2022 at time of writing, as the ISC review process runs about 23–24 months behind real time. We therefore choose to only include earthquakes from 1995-2022 to achieve a stable data set and the best possible results. Our tests on the previously relocated intermediate-depth earthquake catalogues derived for Peru and northern Chile (A. Blackwell *et al.* 2024), when removing earthquakes from >2022, indicate that 25.5 per cent (8815 out of 34 598) of all *ad-hoc* arrays fail due to a lack of reported *P* arrivals. This converts into a loss of

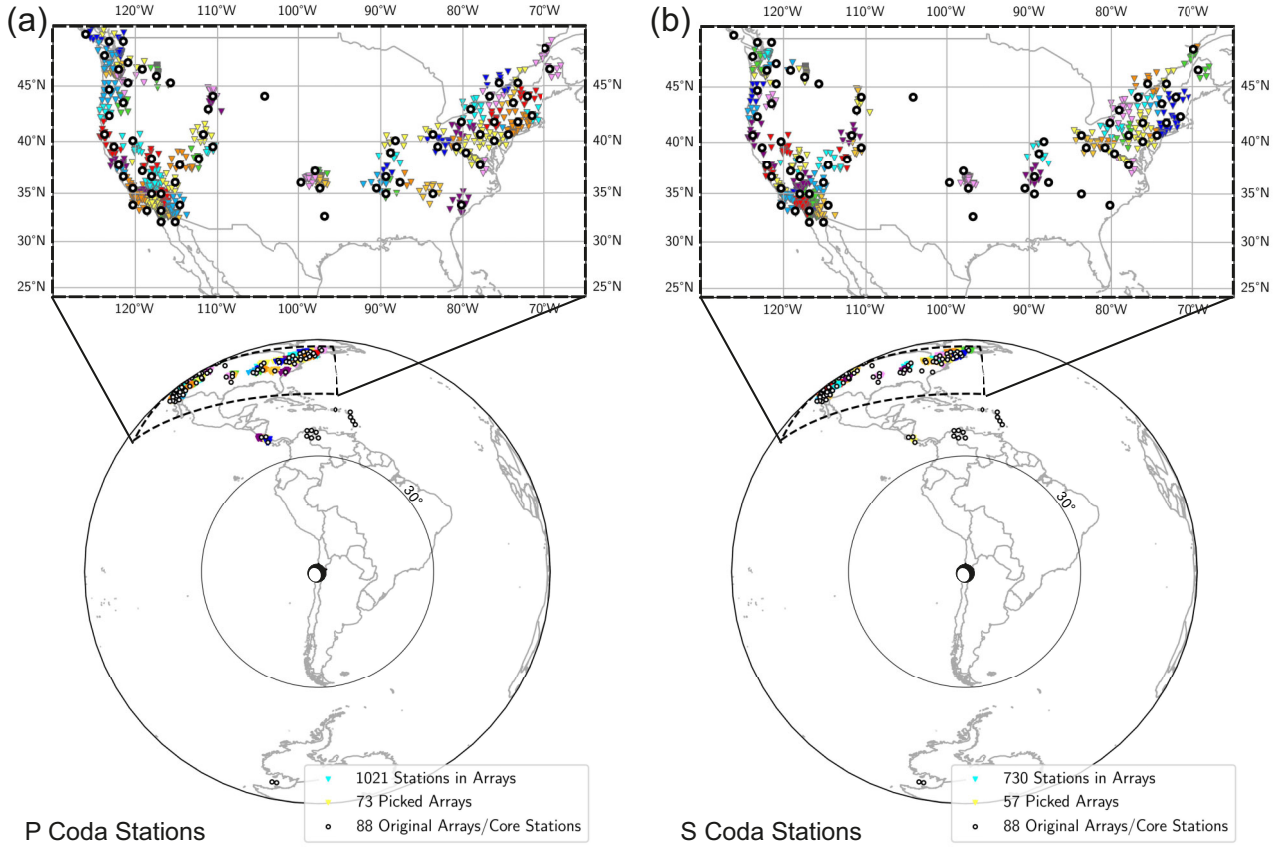

Figure 9. Global distribution of teleseismic stations in picked Z (*P* coda, a) and T (*S* coda, b) component *ad-hoc* arrays (bottom), and a zoom in of the USA *ad-hoc* arrays (top), from the m_b 6.0 2016 July 25 earthquake. The initially created core stations per *ad-hoc* array are shown as thick black circles and the stations of picked *ad-hoc* arrays as coloured triangles. The earthquake focal mechanism is taken from the Global Centroid Moment Tensor Project (GCMT) (A. Dziewonski *et al.* 1981; G. Ekström *et al.* 2012).

11.6 per cent earthquakes, where there are no *P* arrivals within the aperture of any of the *ad-hoc* arrays reported in the ISC catalogue, with a mean magnitude of m_b 4.99. We feel that the failure rates are manageable given the large initial data set, and note that our catalogue will likely have a higher magnitude of completeness than originally intended.

We extend this methodology to the *S*-wave coda picks, using exactly the same approach, except ISC reported *S* arrivals are slowness corrected and used to convert the amplitude-based *S* and *sS* picks to onset times. Both corrections are limited by the availability of direct *P* and *S* arrivals within a given *ad-hoc* array aperture, with *S* coda arrivals rarely being converted as a result. The example earthquake from the 2016 July 25 only had 28.7 per cent of *ad-hoc* arrays with *S* coda picks fail to be converted. However, 92.5 per cent of all candidate T-component *ad-hoc* arrays with picks for the SASZ fail as they have too few reported direct *S*-wave arrivals, resulting in 80.0 per cent of earthquakes with *S* coda picks without a single converted phase. For comparison, only 25.0 per cent of Z-component *ad-hoc* arrays with picks fail to be converted to absolute time, which translates to 22.2 per cent of earthquakes. This illuminates an emerging issue with the low numbers of *S* waves reported by global seismic monitoring agencies.

We find a modal average delta of 0.87 s between the ISC derived *P* arrival and the *ad-hoc* array derived *P* amplitude pick, using the *ad-hoc* arrays from the Peruvian and north Chilean relocated catalogues from A. Blackwell *et al.* (2024) (Fig. S1d). To utilize the *ad-hoc* arrays without a recorded *P* arrival, it might be possible to use the mode to correct the *ad-hoc* array phases to onset times. Alternatively there is the possibility to use a machine learning picker to backfill *ad-hoc* arrays missing a recorded *P* onset. For this paper, we limit our onset correction to the use of the manually reviewed ISC catalogue *P* phases to ensure high quality results.

2.5 Set up and application of ISCloc

The online ISC Bulletin is dynamic, with the possibility of having new phases reported and added for a given earthquake after an ISC hypocentre is determined. In order to appropriately quantify the impact that adding *ad-hoc* array derived depth phases has on earthquake hypocentres, we run ISCloc twice, once with the phases currently reported for an earthquake in the ISC Bulletin, and once with the ISC reported phases plus the onset corrected *ad-hoc* array picks for *P*, *pP*, *sP*, *S* and *sS*, to ensure a fair comparison between the relocation outputs. We exclude ISC reported phases which are observed over 120° away from the ISCloc inputs to avoid complications with core depth phases, and we apply a linear inversion approach which seeds on the published ISC hypocentre. In line with I. Bondár & D. Storchak (2011), we require a minimum of five depth phases to secure depth resolution, and the ability to search/iterate without a fixed initial depth. This criterion is important since the addition of *ad-hoc* array phases could make the difference between

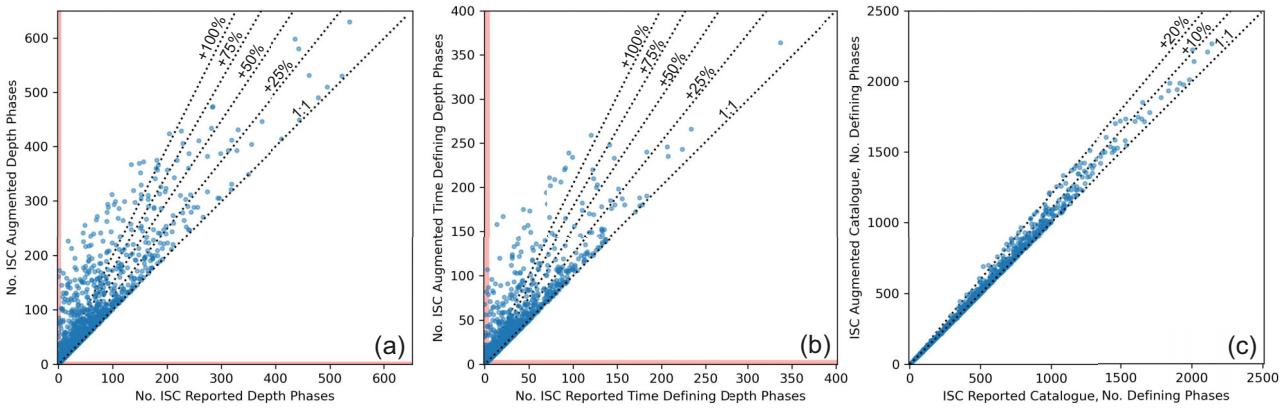

Figure 10. Number of input depth phases (a), time-defining depth phases (b) and all time-defining phases (c) for the ISC reported catalogue versus the augmented ISC catalogue. Red bands highlight earthquakes with less than five depth phases.

an earthquake being located with a fixed, grid defined depth or not, or even from having a robust hypocentre determined at all.

3 CATALOGUE ANALYSIS AND INTERPRETATION

3.1 Assessing the impact of automatically derived depth phases

In this section we will compare the results from ISCloc when inputting the phases reported in the ISC Bulletin, versus the same input plus the *ad-hoc* array determined onsets for *P*, *pP*, *sP*, *S* and *sS*, for each earthquake. Henceforth, we refer to the online ISC Bulletin phases as the reported ISC inputs, and the ISC reported phases with the *ad-hoc* array phases will be referred to as the Augmented ISC inputs. The aim is to assess how the addition of automatically derived depth phases affects both the hypocentre of a given earthquake and the error statistics.

A total of 1694 earthquakes have been augmented with 68 075 additional *ad-hoc* array derived phases, which provide a 50.0 per cent increase in the total number of depth phases used. 27.0 per cent of these depth phases can be fitted within a small enough time residual to inform the relocation. For a phase to be considered by ISCloc, the traveltime residual must be less than four times the expected standard deviation, so for depth phases this is less than or equal to 5.2 s (I. Bondár & D. Storchak 2011). If the traveltime residual is within this range it is considered time defining and therefore informs the earthquake hypocentre, potentially improving the depth resolution (Fig. 10). The percentage of depth phases used to define the hypocentres is low suggesting that ISCloc acts as another quality control upon the depth phases, only allowing picks which agree with the determined epicentre to influence the inversion. Figs 10(a) and (b) also illustrate that the earthquakes with lower numbers of depth phases experience the greatest impact from the addition of *ad-hoc* array derived phases, as the numbers of (particularly time-defining) phases can increase by more than 100 per cent, thus allowing greater depth resolution during the earthquake relocation. We will assess the value of the *ad-hoc* array phase additions in terms of hypocentre location and depth, the associated errors and the relation to earthquake magnitude in this section.

As a result of the incorporated *ad-hoc* array derived phases, there are 1057 earthquakes in the new SASZ intermediate-depth earthquake catalogue with free hypocentre solutions. For the earthquakes which were not relocated, most (784) fail to be relocated due to a lack of *P* and *S* picks reported in the ISC Bulletin, which are required to convert the amplitude picks to onset times. This is especially true for 2023/2024 earthquakes which are not currently considered for conversion (255 earthquakes with picks). An alternative independent method of reporting direct arrivals is needed to improve this in the future, potentially making use of machine learning seismic picking techniques (J. Münchmeyer *et al.* 2024). 79 earthquakes also have had their number of depth phases increased to more than 5, which allows ISCloc to solve for depth (assuming 5 depth phases are time defining) when *ad-hoc* array determined phases are incorporated. The addition of *ad-hoc* determined phases has decreased the mean depth error by 0.47 km (see Fig. 11) when compared to the reported ISC catalogue (relocated using ISCloc and the reported ISC phases, without any additional phases), with depth error reductions for 939 (88.8 per cent) of the 1057 earthquakes.

Depth errors are also unchanged for 68 earthquakes (6.4 per cent), increase for 15 earthquakes (1.4 per cent) and are newly determined for 34 (3.2 per cent) earthquakes which now have a resolved depth due to the incorporation of *ad-hoc* array determined depth phases (i.e. taking them over the threshold value of 5 defining depth phases). The distribution of *ad-hoc* arrays is variable but is typically dominated by *ad-hoc* arrays in North America and Europe due to the available station density and the epi-central distance constraints. Success rate of individual *ad-hoc* arrays depends on local conditions (e.g. noise) and is difficult to predict. Due to these limitations, azimuthal coverage of additional depth phases is variable, but inclusion of a few depth-determining phases into ISCLoc can increase the number of events with determined depth in the relocated catalogue. The earthquakes which have newly resolved depths have an average magnitude of m_b 5.1, average depth of 86.8 km and their epicentres are distributed across the entire SASZ. The few earthquakes with increased error using the augmented ISC catalogue input are typically caused by the additional time-defining phases producing large time residual misfits to the final hypocentre. Given our depth errors can increase when an earthquake has new input phases, it could be suggested that the errors defined for earthquakes are overly optimistic and

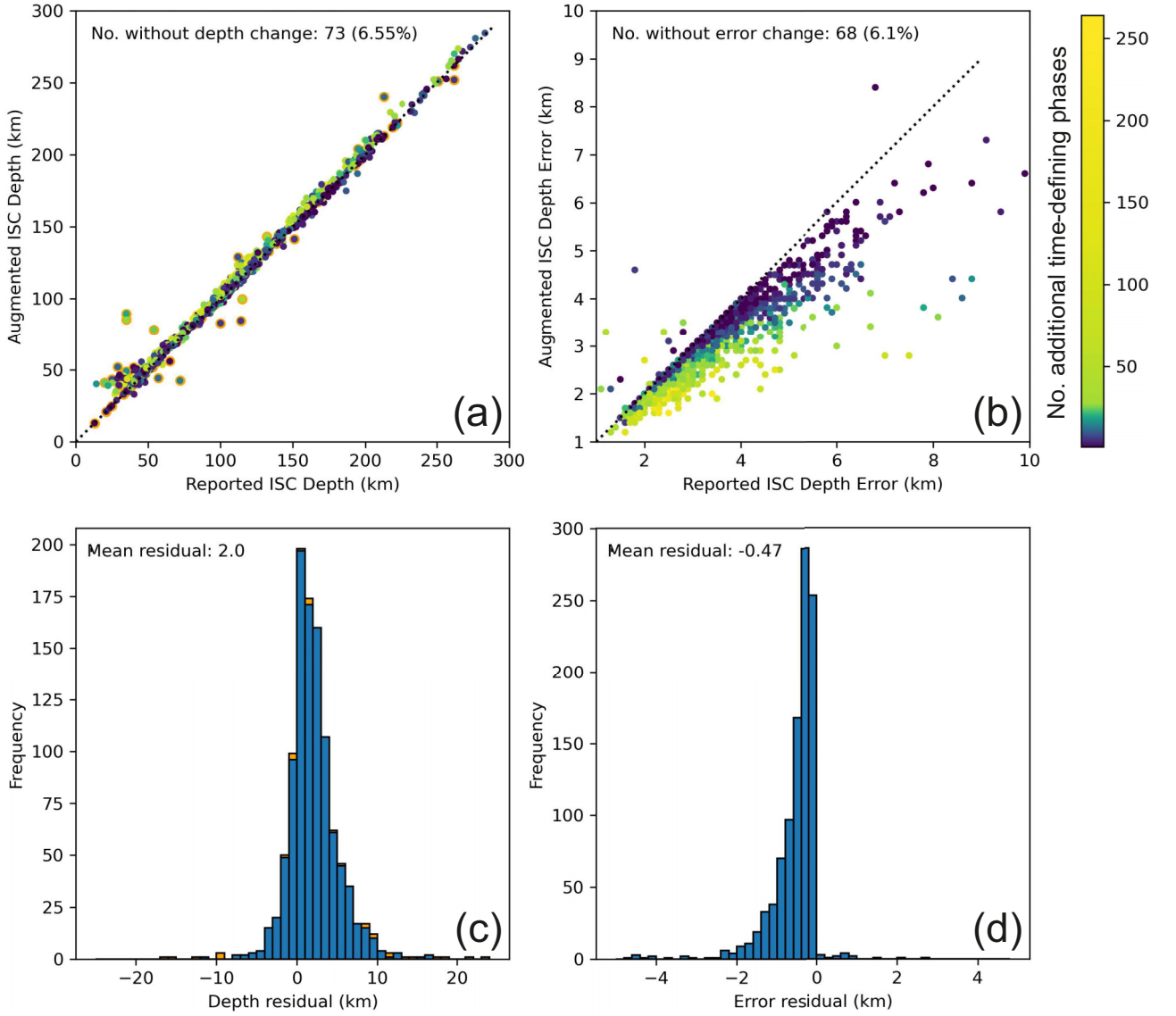

Figure 11. Comparison of depth and depth error between the reported ISC and augmented ISC inputs when applying ISCloc. (a) and (b) show the depth and depth error change when additional *ad-hoc* array phases are included. Both plots are coloured by number of additional time-defining phases, and (a) also has orange outlines for earthquakes which had fixed depths prior to the addition of phases. (c) and (d) are histograms showing the residual between the reported ISC and augmented ISC depths and depth errors, respectively. (c) has orange bars indicating residual in depth when the fixed earthquakes are included. earthquakes which did not have new time-defining phases from the augmented ISC input are not plotted.

need to be increased to align with our error observations in the future.

We additionally note that a reduction in depth error is strongly correlated with the percentage increase in time-defining depth phases, which is largely a function of earthquake magnitude, and not necessarily related to an absolute number of additional phases (Figs S2b and c). Lower magnitude earthquakes are more likely to experience a greater percentage increase in time-defining depth phases, which translates to a greater reduction in depth error. Therefore augmenting the catalogue with *ad-hoc* array derived phases has a greater impact upon the relocations of earthquakes with low numbers of time-defining depth phases, which tend to be low magnitude earthquakes.

We also consider horizontal error reduction by calculating the area of the horizontal error ellipse, and note that the addition of *ad-hoc* array phases minimally influences the horizontal error, with a mean reduction of 1.95 km^2. Despite this, some outliers exist where the horizontal error significantly decreased—notably there is an earthquake showing a reduction of 144 km^2. Further inspection of these examples shows that time-defining *sP* additions with small time residuals allow significant horizontal error reduction when few depth phases exist in the ISC reported catalogue, and the hypocentre was already poorly constrained; the example with the 144 km^2 reduction had an initial horizontal error area of >800 km^2. This suggests that improvement of horizontal and depth error is more sensitive to added *sP* than *pP* phases.

We test the sensitivity of depth error reduction to the addition of *pP* versus *sP* (see Fig. S3). We find that a greater absolute number and proportion of *sP* phase additions compared to *pP* phase additions lowers the depth error for earthquakes

by a mode of 0.14 and 0.71 km, respectively. It is clear that a reduction in depth error benefits from a larger number of *sP* phases, likely due to the low numbers in the reported ISC catalogue compared to the number of reported *pP* phases. The greater impact of sP phases on the depth resolution may also be because a shift in depth will have a greater effect on the relative timing of the sP phase due to the s leg of the sP phase travelling slower than the 'p' leg of pP.

3.2 Continental-scale application—South American Subduction Zone

The previous section has shown that a proportional increase in *P*, *pP*, *sP*, *S* and *sS* phases—determined through *ad-hoc* arrays—decreases the number of earthquakes where depth is defined from a pre-determined grid (fixed), decreases depth error in 88.8 per cent of earthquakes and that *sP* phase additions influence the reduction in depth error to a greater extent than *pP*. Whilst the reductions are typically small (mean reduction of 0.47 km), slight improvements in depth resolution across an earthquake catalogue can allow updates in the interpretation of a seismogenic region.

Fig. 12 shows the new intermediate-depth earthquake catalogue for the SASZ, determined with the augmented ISC phase catalogues and ISCloc, with example cross-sections highlighted [see supplementary material for figures showing all of the example cross-sections, and a map of depth change between the reported and augmented ISC catalogues (Fig. S12)]. Cross-sections C–C', D–D' and I–I' (Fig. 13) illustrate the differences between the earthquake hypocentres with and without the *ad-hoc* array determined phases, and when the phase catalogues are only augmented with the *P* coda picks. They also show previously identified features along the SASZ, including the Peruvian flat slab (D. Portner & G. Hayes 2018) and Pucallpa nest (C–C') (L. Wagner & E. Okal 2019; D. Sandiford *et al.* 2020), the transition from flat to normally dipping slab in northern Chile (D–D') (L. Ye *et al.* 2020), the geometry of the Pampean flat slab (N. Flament *et al.* 2015) and how the apparent seismogenic slab thickness can be decreased when the *ad-hoc* array derived phases are incorporated into the earthquake relocation (I–I').

The cross-sections shown in Fig. 13 also demonstrate the limited effect including *S* and *sS* has on earthquake relocations. This is largely due to the relatively small number of *S* coda phases which were converted to absolute onset times, in order to use them with ISCloc. Only 830 *sS* phases were added to the reported ISC phase catalogues, compared to 20 196 *pP* and 20 442 *sP* phases (see Fig. 10 to compare phase additions). However, 229 *ad-hoc* array derived *sS* phases became time-defining for the ISCloc hypocentre solutions, this forms 49.7 per cent of the total time-defining *sS* phases and indicates that whilst the final *sS* phases numbers are currently small, they are enhancing the reported ISC catalogue, although, the inclusion of *S* and *sS* does not currently translate to large depth error reductions. To demonstrate this quantitatively, the augmented catalogue using both *P* and *S* coda arrivals, and the augmented catalogue using only the *P* coda phases have the same mean depth error reduction relative to the reported ISC catalogue (0.47 km), and nearly the same mean residual (2.00 and 1.98 km, respectively) between the augmented and reported ISC earthquake depths when *ad-hoc* array determined phases are incorporated (see Figs 11 and S4).

We compare our new catalogue to the published ISC Bulletin and NEIC catalogues for the region in Fig.14 The selected cross-sections indicate an aseismic gap at subduction depths of $<$90 km in the plate between two planes of seismicity, which further supports the presence of a DSZ in Chile. Section G–G' additionally displays an aseismic gap between approximately 380–420 km distance from the trench.

Although hypocentre differences between the published ISC catalogue and our catalogue are small (mean depth difference 0.51 km), improvements in depth error determination can be seen clearly for two earthquakes closest to the trench on section E–E' and for the deepest earthquake on section G–G', where the published ISC catalogue has failed to determine a depth error due to insufficient depth resolution and our augmented catalogue has succeeded. However, the ISC published catalogue does demonstrate smaller depth errors by a mean of 0.3 km than our unsupervised ISCloc results (see Fig. S14). This demonstrates the value of human seismic analysts during the relocation process.

The NEIC catalogue generally demonstrates a larger scatter in seismicity, larger seismogenic thickness and larger depth errors than both our and the published ISC catalogues, where independently determined earthquake depths are indicating more discrete, linear slab features. The mean depth difference between the NEIC published catalogue and our augmented ISC catalogue is 1.95 km (see Fig. S15), and our catalogue reduces depth error by a mean of 0.93 km, whilst demonstrating a maximum reduction of 5 km. All example cross-sections indicated on the map in Fig. 12 can be seen in the supplementary material with both the ISCloc comparison and published catalogue comparison versions.

It is also worth noting that published slab interfaces (Slab 1.0 and Slab2) seem not to fit the indicated slab behaviour from the new catalogue. For distances greater than 400 km from the trench, both the Slab 1.0 (G. Hayes *et al.* 2012) and Slab2 models (G. Hayes *et al.* 2018) indicate that subducting slab thicknesses of up to 50 km exist between the slab interface and the intermediate-depth earthquakes (Figs 13 and 14). Given that oceanic crust thickness is typically approximated to be 7 km, and intraslab earthquakes occur in the slab crust and/or upper mantle (G. Abers *et al.* 2013), a separation of over 20 km between the proposed interface above an intraslab earthquake implies a poorly fitting slab interface model (Fig. S13; (K. Wang 2002)). In such cases, the slab interface needs to be deepened, bringing it into line with high-accuracy intraslab seismicity, to prevent interpretation of an overly thick aseismic top to the slabs.

3.2.1 *Structure of the Wadati–Benioff Zone in northern Chile*

We use the resultant high resolution earthquake catalogue to investigate the structure of the Wadati–Benioff zone (K. Wadati 1935; H. Benioff 1949) in northern Chile, where a double seismogenic zone has been previously proposed by both C. Sippl *et al.* (2018) and M. Florez & G. Prieto (2019). Two Chilean cross-sections (Fig. 14) using the new earthquake catalogue qualitatively support the presence of a double seismic zone, when considered in tandem with local microseismicity data (C. Sippl *et al.* 2018). Using these cross-sections, we interpret a broad convergence zone where the planes cannot be resolved, which ranges from approximately 100–160 km in depth. This corroborates the previously hypothesized 80–120 km deep convergence depth for

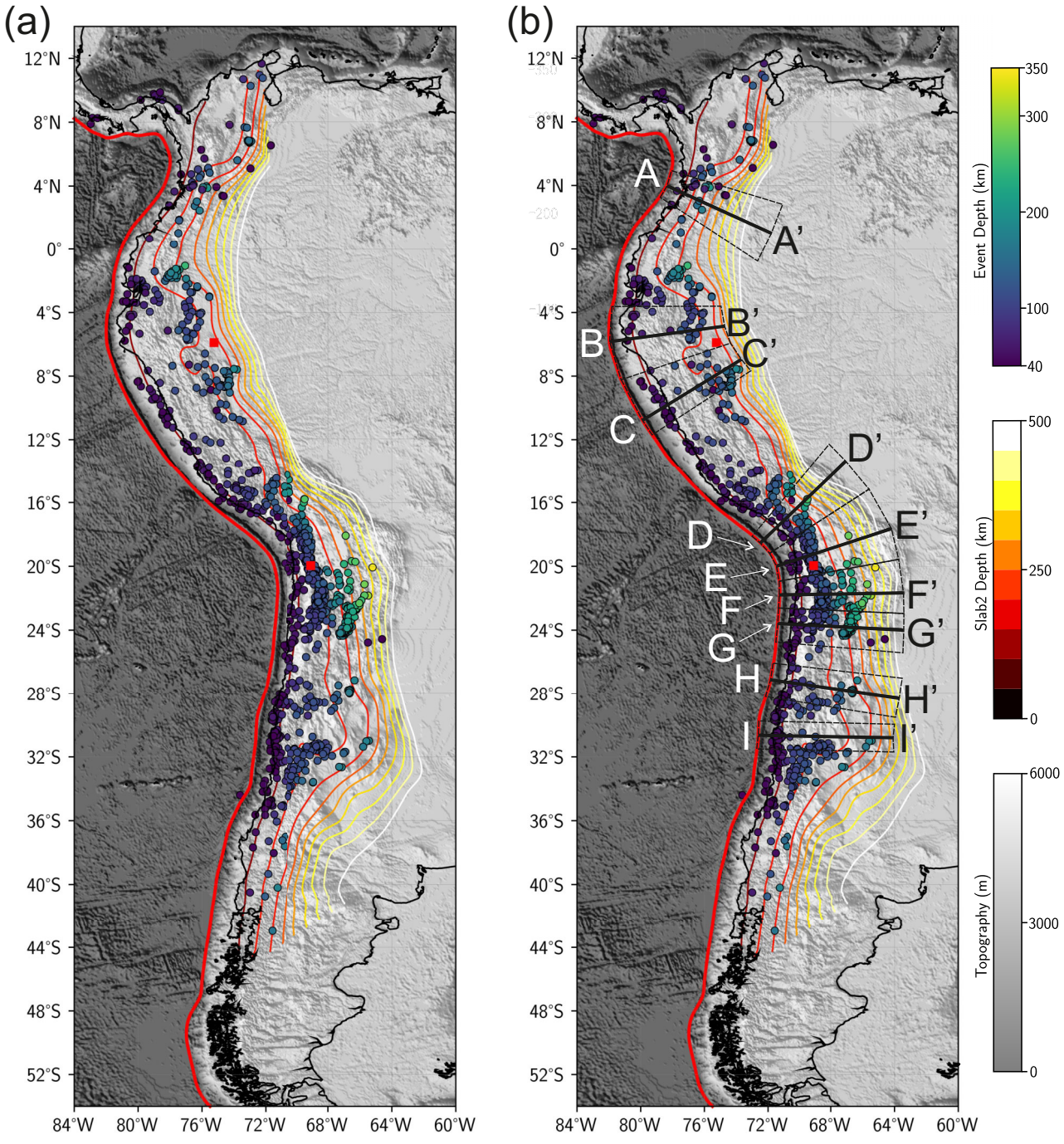

Figure 12. Map of the relocated intermediate-depth earthquakes (a), using the ISC augmented phase catalogues (which include *ad-hoc* array determined *P*, *pP*, *sP*, *S* and *sS* phases), with Slab2 contours (G. Hayes *et al.* 2018) and cross-section locations (b). Red squares indicate the M_w 8.0 Peruvian earthquake and M_w 7.7 Tarapacá earthquake (Section 3.3).

this latitude of the Nazca subducting slab using microseismicity observations (C. Sippl *et al.* 2018, 2023), and the 142.1±8 km convergence depth found using relatively relocated teleseismic data (M. Florez & G. Prieto 2019) and ak135 (B. Kennett *et al.* 1995). Variation between our augmented catalogue depths and the C. Sippl *et al.* (2018) catalogue is expected since our data set is derived using a different velocity model, and therefore will suffer a translational offset in depth relative to the microseismicity catalogue.

To quantitatively investigate the presence of a double seismogenic zone we follow the work of M. Brudzinski *et al.* (2007), who use slab normal hypocentre locations above the point of double seismogenic zone convergence to determine if a two-layer, bimodal distribution exists. Figs 15(a) and (b) show sections E–E' and G–G' with both the augmented catalogue earthquake hypocentres and the local Sippl microseismicity catalogue (C. Sippl *et al.* 2018), and their lines of best fit. The lines of best fit are subsequently used to correct the earthquake depths relative

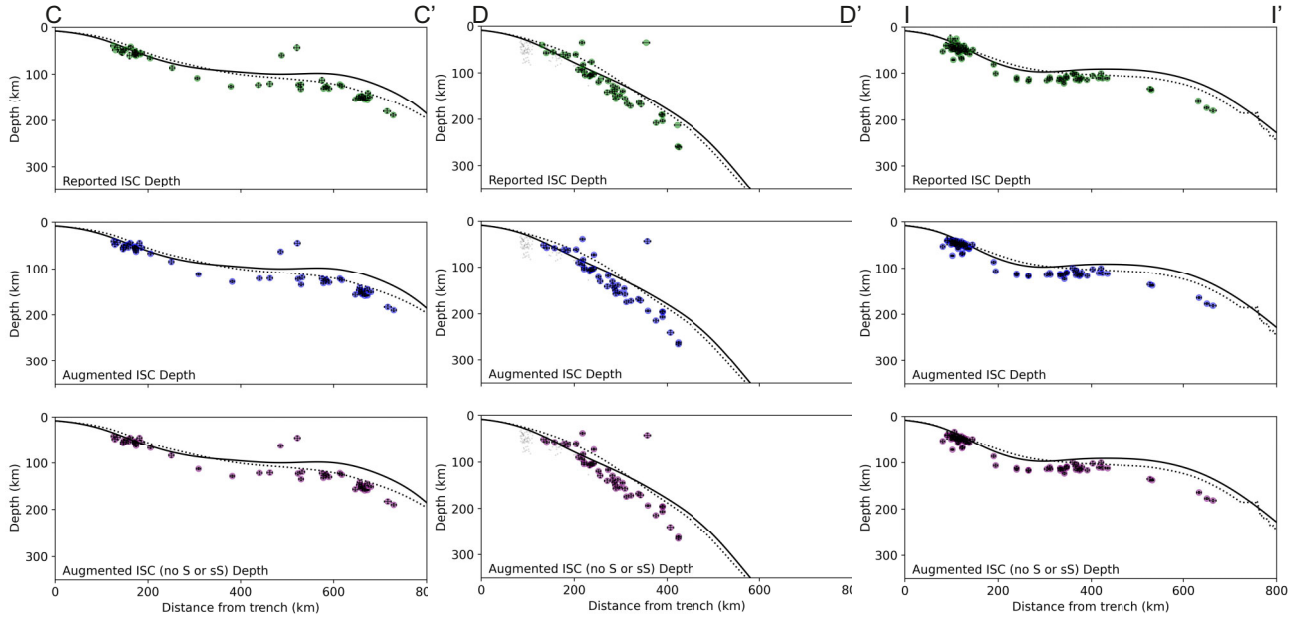

Figure 13. Example cross-sections showing slab features, and differences between the earthquake catalogues determined using only the ISC reported phases (top), the ISC catalogue augmented with *P* and *S* coda picks (middle), and ISC catalogue augmented with only the *P* coda picks (bottom). Note that *P* coda picks refers to *P*, *pP* and *sP*, and *S* coda picks refers to *S* and *sS*. Horizontal and depth error bars are plotted per earthquake, and are often within the symbol diameter. Slab2 is plotted as a solid black line and Slab 1.0 is plotted as the dotted black line for comparison. Cross-section locations shown in Fig. 12

to the seismogenic slab geometry, and find the slab normal distribution of the hypocentres–shown in (b) and (d). The C. Sippl *et al.* (2018) catalogue here is limited to earthquakes categorized as either lower plane, upper plane or plate interface classes, in order to avoid loss of resolution from earthquakes which are not thought to form the double seismogenic zone. We note that these earthquake categories, on the cross-sections we inspect, end at approximately 230 km from the trench where plane convergence is expected, we therefore also limit the augmented ISC catalogue and calculate the linear lines of best fit only for earthquakes within 230 km of the trench.

From these, we demonstrate an incipient bimodal distribution in both cross-sections from the C. Sippl *et al.* (2018) data set, with a 20–30 km seismogenic gap apparent, although the lower plane seismicity is underdeveloped relative to the upper plane for both. The augmented ISC catalogue shows a weaker bimodal distribution in Fig. 15(b), with a more strongly defined lower plane and an approximately 20 km seismogenic gap. Whereas section G–G' on Fig. 15(d) lacks enough earthquakes to define a confident histogram, yet still hints at bimodal distribution when considered in conjunction with the C. Sippl *et al.* (2018) catalogue slab normal distributions, despite offsets in both sections due to the use of different velocity models.

Whilst individually the augmented, high resolution catalogue results are not conclusive enough to determine a double seismogenic zone, we believe that their results corroborate the presence of two planes seen in the microseismic data. Our findings reflect the resolution of the global catalogue determined histograms in M. Brudzinski *et al.* (2007), where maximum frequencies of 15 or 16 earthquakes define the north east Japanese double seismic zone with an approximately 30 km aseismic gap. The confidence in the global catalogue observed double seismic zones is increased when compared to the histogram resulting from the local catalogue (with maximum frequencies of 182 earthquakes), similarly to our comparison to the C. Sippl *et al.* (2018) catalogue histograms.

The M. Brudzinski *et al.* (2007) approach allows us to assess the likely presence of a double seismogenic zone, however to characterize the geometry and plane seismicity to a greater degree of accuracy using teleseismic data sets, the approach of M. Florez & G. Prieto (2019) could be reproduced. Their use of relative relocation, following the double difference methodology, to define their earthquake catalogue allows the hypocentres to align along a coherent slab geometry, and enables further analysis, such as investigating the controls upon the width of the aseismic gap and depth of double seismic plane convergence. For northern Chile, M. Florez & G. Prieto (2019) determine an 11.1–11.7 ±4 km wide average aseismic gap, these values indicate that our slab-corrected augmented ISC catalogue and histogram driven results lack the precision to resolve a high accuracy measurement and likely mask a smaller aseismic gap. To continue research into the Chilean double seismogenic zone, we believe relative relocation of the earthquake hypocentres is necessary to enhance the prevalent slab geometries and ascertain higher degrees of accuracy.

3.3 Comparison with finite-fault studies of major earthquakes

A number of large magnitude earthquakes have occurred at intermediate-depths along the SASZ. From these two stand out–the M_w 8.0 Peruvian earthquake on 2019 May 26 and M_w 7.7 Tarapacá earthquake on 2005 June 13. Although both earthquakes exceed the maximum magnitude at which we apply the approach developed in this paper, the rupture kinematics of these earthquakes have been studied in detail using a combination of backprojection imaging, finite fault modelling and waveform inversion (S. Peyrat *et al.* 2006; B. Delouis & D. Legrand

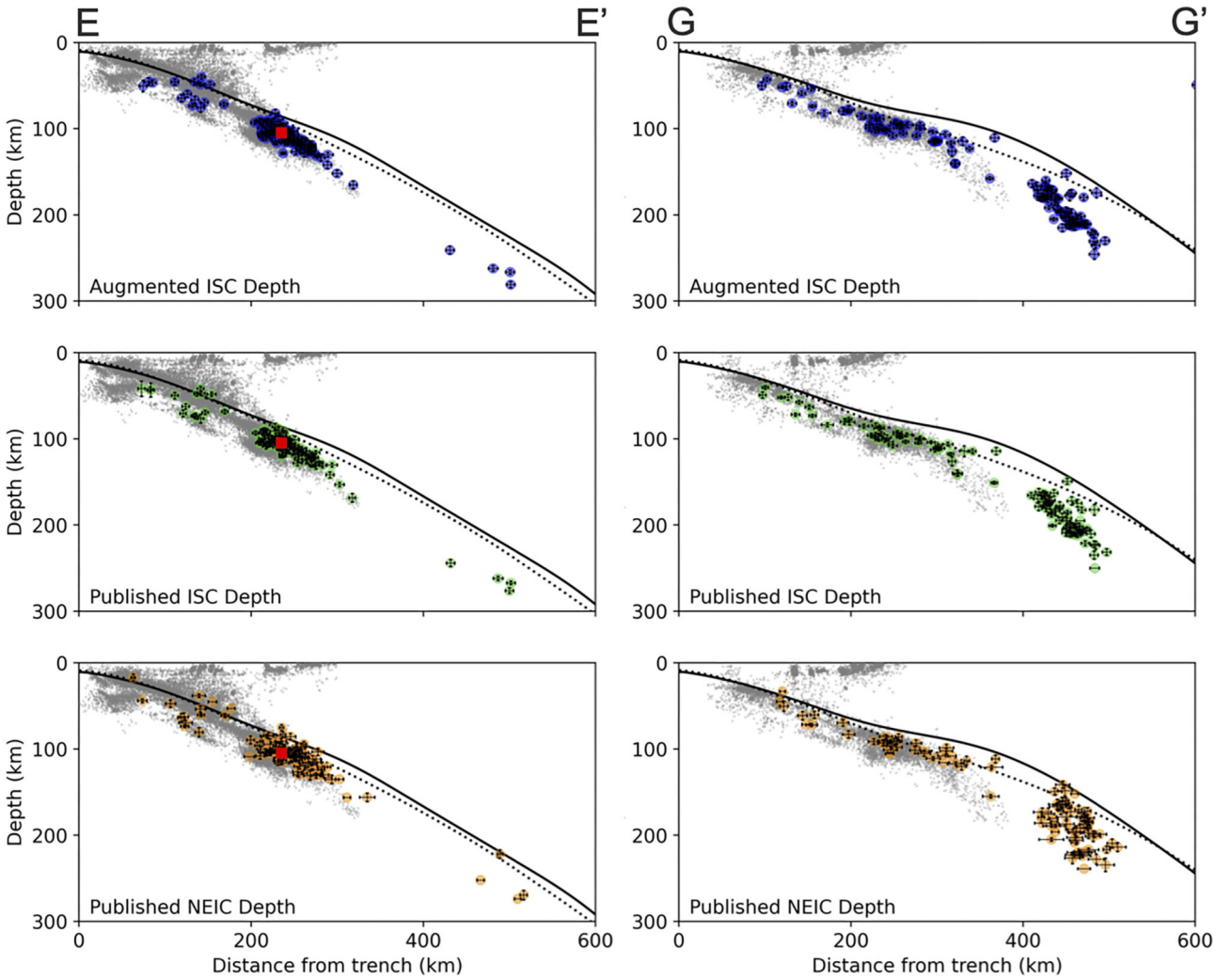

Figure 14. Example cross-sections showing the difference between the augmented ISC catalogue from this study (top), published ISC earthquake catalogue (middle) and published NEIC catalogue (bottom). Horizontal and depth error bars are plotted per earthquake, they are often within the symbol diameter. Slab2 is plotted as a solid black line and Slab 1.0 is plotted as the dotted black line. Cross-section location shown in Fig.12 Red square shows location of M_w 7.7 Tarapacá earthquake (Section 3.3).

2007; K. Kuge *et al.* 2010; L. Ye *et al.* 2020; W. Liu & H. Yao 2020).

3.3.1 M_w 7.7 Tarapacá earthquake

The 2005 M_w 7.7 Tarapacá earthquake occurred in the upper plane of the double seismic zone of northern Chile. Finite-fault studies of this earthquake using combined seismic and geodetic data conclusively show that it ruptured on a subhorizontal, west-dipping plane, in an orientation consistent with the reactivation of faults from the outer rise (S. Peyrat *et al.* 2006; B. Delouis & D. Legrand 2007). The earthquake was followed by a strong aftershock sequence (defined here as earthquakes post dating the main shock). Many of the aftershocks have been relocated here using our new approach. Our improved hypocentres for moderate-magnitude seismicity delineate a clear subhorizontal plane of seismicity in the source region of the Tarapacá earthquake, spanning roughly the same spatial extent as the downdip width of the best available finite fault model from the USGS (G. Hayes 2017). The USGS finite fault model is nucleated on the hypocentre from the NEIC PDE (white diagonal line, Fig. 16), which is ∼ 13.5 km further west than the ISC located hypocentre. Applying a similar shift to the entire finite fault model would result in a close match between the extent and orientation of the finite fault model and the aftershock cloud. The aftershocks perhaps suggest a slightly shallower dip than used in the finite fault inversion. In this case, it is clear that the M_w 7.7 earthquake ruptured the full width of the upper seismic zone, which hosts the vast majority of seismicity with $m_b > 4.7$, and perhaps extended further into the aseismic region separating double seismic zones than is usually seen. However, it did not reach the lower seismic zone, which at these depths is only really apparent thanks to the dense microseismic networks available in northern Chile.

3.3.2 M_w 8.0 Peruvian earthquake

The 2019 M_w 8.0 intraslab earthquake beneath Peru has been well studied (e.g., Y. Hu *et al.* 2021; M. Vallée *et al.* 2023; L. Zeng *et al.* 2025). In Fig. 16(c), we show the finite fault models of L. Zeng *et al.* (2025) for comparison with our relocated moderate-magnitude seismicity, with the furthest east being the 2019 M_w8.0 earthquake.

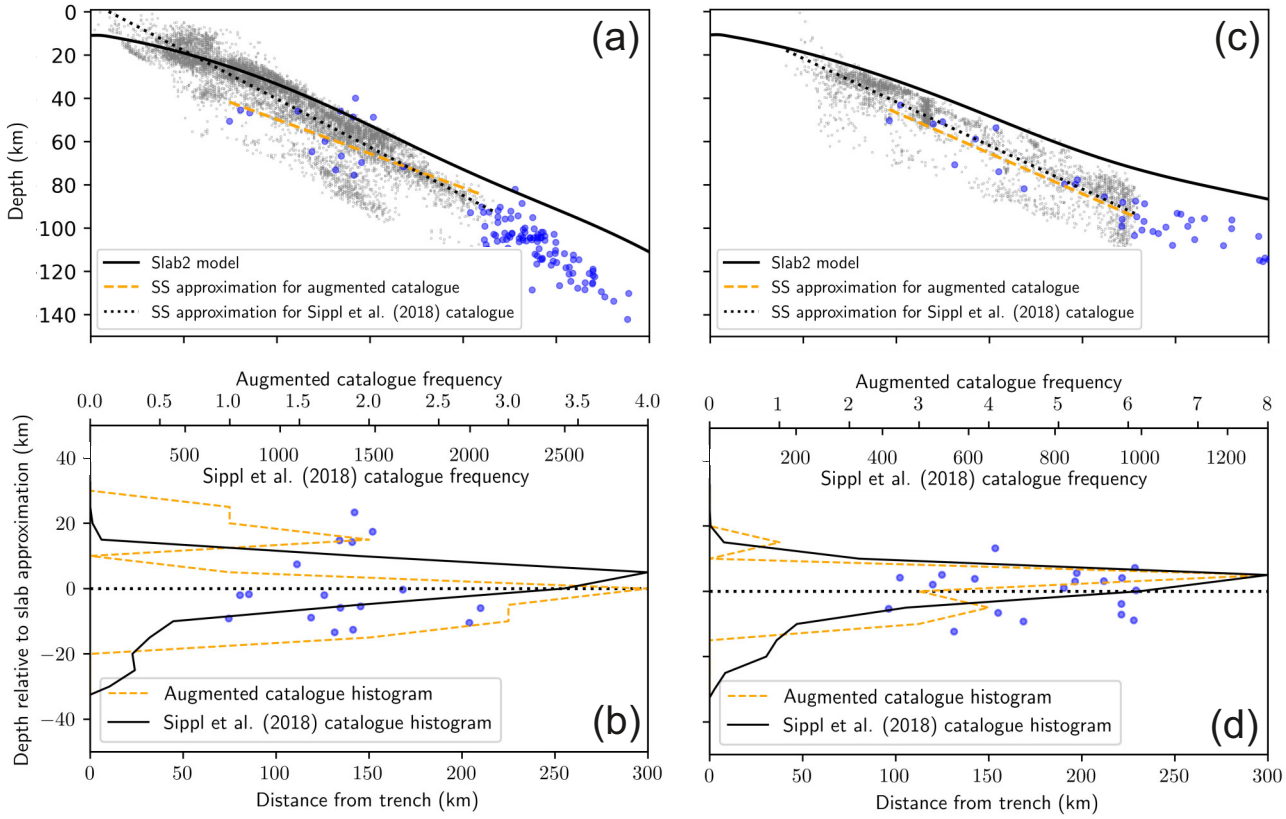

Figure 15. Zoomed-in E–E' (a) and G–G' (c) cross-sections of the northern Chilean subducting slab, showing the augmented ISC catalogue (blue circles) and C. Sippl *et al.* (2018) catalogue (small grey circles) seismicity from the trench to 300 km inland, with seismogenic slab (SS) approximations for each catalogue. Slab 1.0 (G. Hayes *et al.* 2012) and Slab2 models (G. Hayes *et al.* 2018) shown in dotted and solid black, respectively. Histograms showing slab normal distributions of the augmented ISC and C. Sippl *et al.* (2018) catalogues for the E–E' (b) and G–G' (d) cross-sections. Fig. 12 shows the location of the sections on a map of the SASZ.

In contrast to the more productive aftershock sequence of the Tarapacá earthquake, the Peruvian earthquake had very few aftershocks, in keeping with most intermediate-depth earthquakes (e.g., S. Wimpenny *et al.* 2023), with no clear fault plane delineated. H. Luo *et al.* (2023) suggest that this earthquake ruptured through both seismic zones, as determined by M. Brudzinski *et al.* (2007). However, our relocations in this region remain insufficient to clearly distinguish a separation into two seismic zones. Whilst we lack the resolution to separate the earthquake population into distinct seismic zones, the depth-extent of rupture (L. Zeng *et al.* 2025) is similar to the depth range over which we see moderate-magnitude seismicity distributed in our relocations.

The hypocentre location and mechanism of this earthquake (downdip normal-faulting) suggest that it likely locates at, or near, the point of rebending at the downdip end of the Peruvian flat slab. However, it is more plausibly situated in the initial part of the bend—where the upper section of the plate is accumulating curvature—rather than the 'unbending' section, where the upper plane is instead in downdip compression (e.g. C. Sippl *et al.* 2022; T. Craig *et al.* 2022). Alongside the broad region of moderate-magnitude seismicity slightly further up dip, this suggests that the termination of the Peruvian flat slab is likely to be slightly further east than currently incorporated in slab models (G. Hayes *et al.* 2018). Fig. 16(c) also shows finite fault rupture models for other $M_w \geq 7.5$ earthquakes in the Peruvian flat slab region, from L. Zeng *et al.* (2025). The rupture extent of these earthquake fits with the seismogenic width of the slab indicated by our relocated moderate-magnitude seismicity, indicating that our refined teleseismic hypocentres are now appropriately imaging the seismogenic structure of the slab, suitable of use in constraining maximum magnitudes for seismic hazard.

4 DEEP FOCUS EARTHQUAKES

As described in Section 2, our approach is designed for the relocation of intermediate-depth earthquakes (A. Blackwell *et al.* 2024), and has been shown in Section 3 to increase the resolution of continental-scale earthquake catalogues. Given the relatively low numbers of deep focus earthquakes in the SASZ, and their capacity to enhance the overall understanding of the region, we test the limits of our methodology and additionally relocate these earthquakes.

Using the same time period and parameters in Section 2.1, except with a new search depth of 350–700 km, we find 48 candidate earthquakes in the ISC catalogue. 24 earthquakes were successfully relocated, from the array processing stages through to the relocation using ISCloc, with 20 earthquakes failing to pass the *ad-hoc* array quality control criteria or have detected phases and 4 earthquakes failing during the step to time-shift the picked phases to absolute onset times. The addition of *ad-hoc* determined phases has decreased the mean depth error by 0.15 km

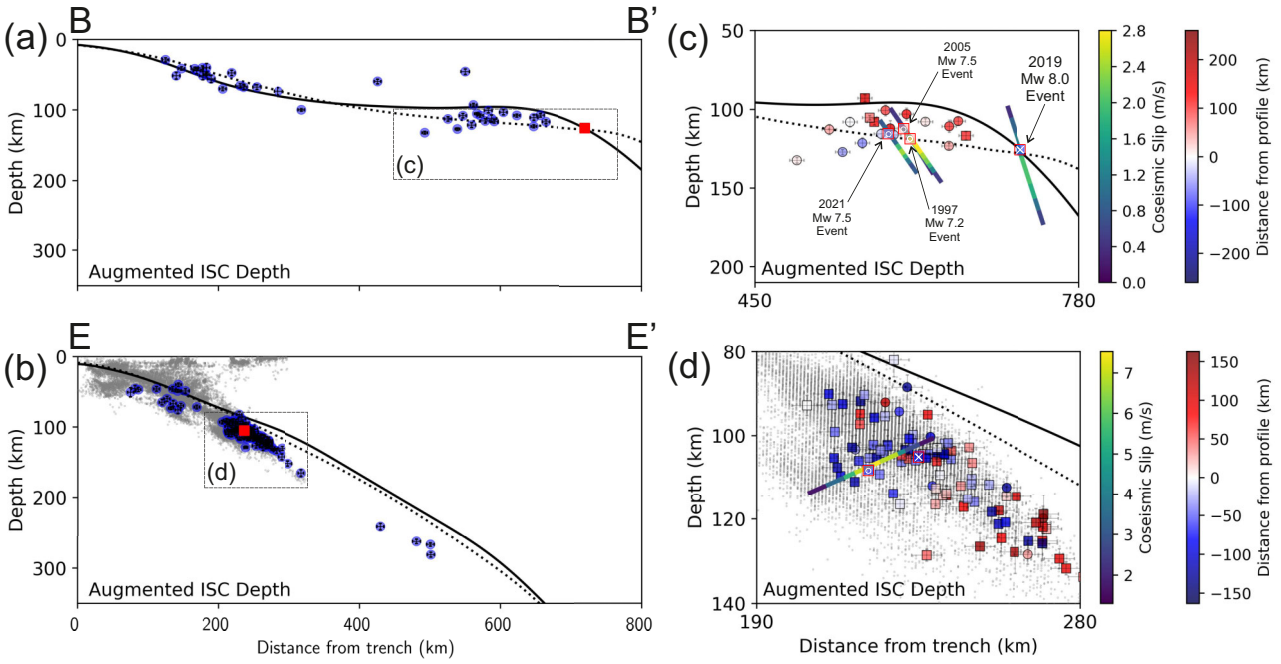

Figure 16. Example cross-sections B–B' and E–E' showing the 2019 M_w 8.0 Peruvian earthquake (a) and 2005 M_w 7.7 Tarapacá earthquake (b) as red squares, alongside the augmented ISC catalogue (blue circles) and C. Sippl *et al.* (2018) catalogue (small grey circles) seismicity (only b/d). (c) and (d) show the earthquakes present in the zoomed-in boxes on (a) and (b), coloured by distance from the cross-section and shown as circles if the earthquake pre-dates the major earthquake, or squares if it post-dates. Major earthquakes are marked by red-outlined squares, with the ISC hypocentres (International Seismological Centre 2024) shown as white crosses and the USGS hypocentres (which are used for the finite fault models) indicated by white circles. Finite fault models from L. Zeng *et al.* (2025) are shown on (c) for earthquakes with $M_w \geq 7.5$, and the G. Hayes (2017) finite fault model is shown on (d) for the Tarapacá earthquake. All finite fault models display the maximum slip along the fault plane, projected onto the cross-sections. Slab 1.0 (G. Hayes *et al.* 2012) and Slab2 models (G. Hayes *et al.* 2018) shown in dotted and solid black, respectively. Fig. 12 shows the location of the sections on a map of the SASZ.

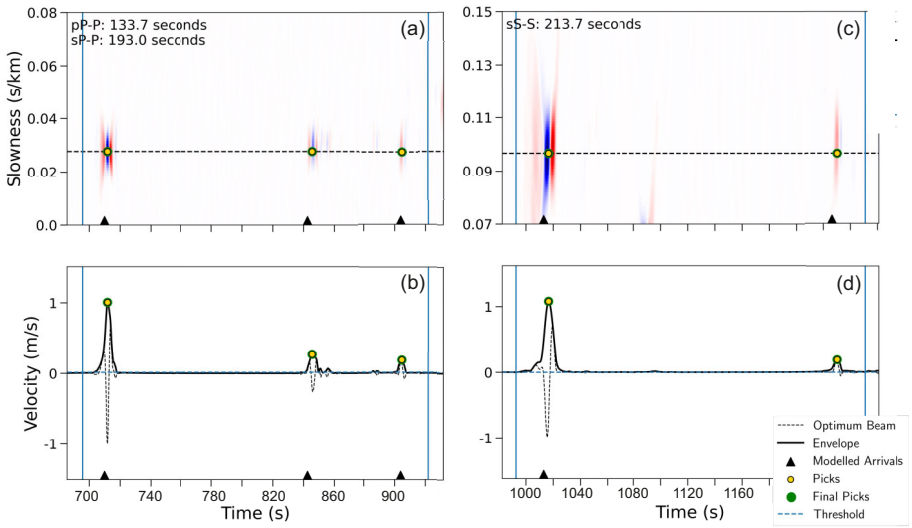

Figure 17. Example Z and T-component *ad-hoc* arrays, their automatic picks and differential times between phases for the deep m_b 6.0 earthquake which occurred on 2022 August 6 in eastern Brazil. (a) and (b) are the vespagram and optimum beam respectively for the Z-component *ad-hoc* array located 88.9° from the earthquake, whilst (c) and d) are the vespagram and beam for the T-component *ad-hoc* array located 61.5° from the earthquake. Blue vertical lines indicate the time window of data used for automatic picking.

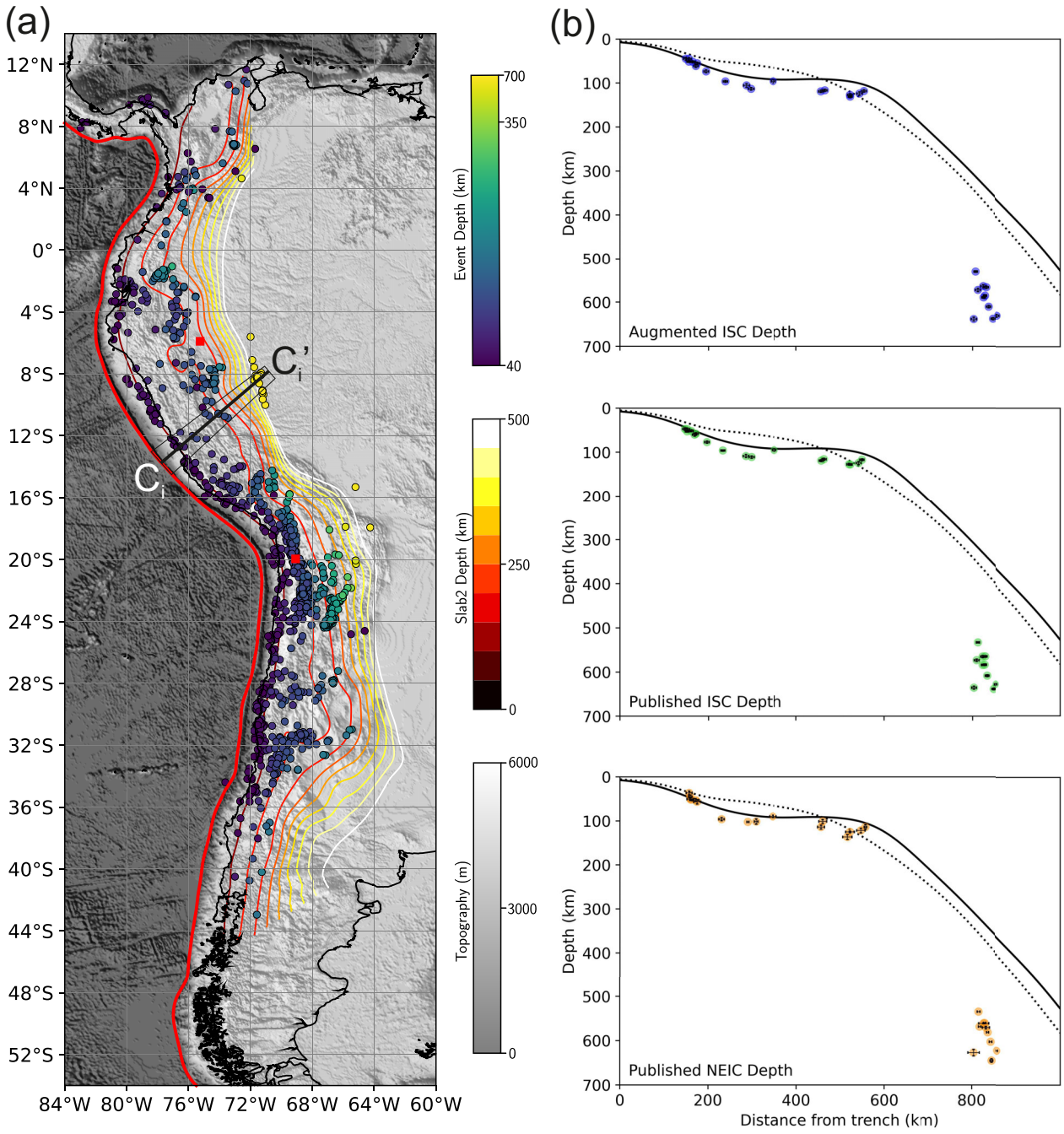

Figure 18. Map with Slab2 contours (G. Hayes *et al.* 2018) (a) and example cross-section (b) of the final SASZ intermediate-depth and deep focus earthquake catalogues. (b) shows the difference between the augmented ISC catalogue from this study (top), published ISC earthquake catalogue (middle), and published NEIC catalogue (bottom). Horizontal and depth error bars are plotted per earthquake, they are often within the symbol diameter. Slab2 is plotted as a solid black line and Slab 1.0 is plotted as the dotted black line. Red squares show hypocentres of the M_w 7.7 Tarapacá earthquake and M_w 8.0 Peruvian earthquake (Section 3.3).

(see Fig. S16) when compared to the reported ISC catalogue (relocated using ISCloc and the reported ISC phases, without any additional phases).

Fig. 17 demonstrates the approach on an example m_b 6.0, deep (619.2 km according to the ISC) earthquake from 2022 August 6. 105 *ad-hoc* arrays with 1728 stations were created from a total of 2400 available teleseismic stations, resulting in 52 *P*, 52 *pP*, 17 *sP*, 1 *S* and 1 *sS* absolute onset picks. From inspection of this and other examples, we believe that the approach works well on deep focus earthquakes and therefore, we include them in our final relocated catalogue. Fig. 18 demonstrates the relocated intermediate-depth and deep focus earthquake catalogues for the SASZ, with an example cross-section. The cross-section clearly shows the need for a deeper slab model with respect to distance from the subduction trench, and allows a more comprehensive understanding of slab geometry inland. Crucially, the ability to successfully use array processing on deep focus earthquakes, and detect small amplitude phases, opens up

opportunity to expand our application of adaptive *ad-hoc* arrays to a broader range of earthquakes.

5 CONCLUSION

The ISCloc intermediate-depth earthquake relocations (solved for hypocentral latitude, longitude, depth and earthquake origin time) based upon the augmented ISC phase catalogue (ISC reported phases with additional automatically-derived *P*, *pP*, *sP*, *S* and *sS* arrivals) for the South American Subduction Zone show a decrease in depth error for 88.8 per cent of earthquakes in our catalogue, and therefore a refinement in hypocentral depths. Significant improvements are particularly evident when comparing previous catalogue relocations based on *ad-hoc* arrays (A. Blackwell *et al.* 2024) to those enhanced by ISCloc, owing to its incorporation of bounce point and elevation corrections, and its simultaneous inversion for hypocentre latitude, longitude and depth. It is clear that automatically determined phase arrivals, from array processed teleseismic data, are a useful resource to the wider community to improve earthquake locations and depths, and enhance interpretation. The greatest limitation of the presented approach is the conversion of the *ad-hoc* array determined amplitude picks to absolute phase onset times. We suggest an alternative method involving machine learning for this conversion, which could be used in future applications.

We use our new earthquake catalogue to investigate the Wadati–Benioff zone in northern Chile. We find that despite the improvements in depth resolution, our teleseismic earthquake catalogue cannot independently verify the presence of a double seismogenic zone in northern Chile, without reference to the local microseismicity catalogue created by C. Sippl *et al.* (2018). We additionally consider two major earthquakes from the South American Subduction Zone—M_w 7.7 Tarapacá earthquake and M_w 8.0 Peruvian earthquake—and evaluate their aftershocks (which have been relocated by our approach) relative to their finite fault models (G. Hayes 2017; L. Zeng *et al.* 2025). Our high-resolution earthquake hypocentres reveal a well-defined subhorizontal plane of seismicity in the source region of the Tarapacá earthquake, extending across approximately the same downdip width as that of the USGS finite fault model (G. Hayes 2017) yet at a shallower dip. In contrast, our catalogue shows few aftershocks of the Peruvian earthquake and does not reveal an associated plane. However, the finite fault model and its proximity to a broad region of seismicity updip suggests that the earthquake is a consequence of early slab rebending. This indicates that the distal bend of the Peruvian flat slab exists eastwards of existing slab models.

Finally, we test our approach by also relocating deep focus earthquakes associated with the SASZ, in order to comprehensively understand the geometry of the subducting Nazca plate. These earthquakes demonstrate a mean depth error reduction of 0.15 km, further validating the findings from the relocated intermediate-depth earthquake catalogue that *ad-hoc* array determined depth phases improve the depth resolution of teleseismic earthquake catalogues.

ACKNOWLEDGMENTS

AB was supported by the Leeds-York-Hull Natural Environment Research Council (NERC) Doctoral Training Partnership (DTP) Panorama under grant NE/S007458/1. TJC was supported in this work by the Royal Society under URF\R1\180088, URF\R\231019 and RF\ERE\210041, and also through COMET, which is the NERC Centre for the Observation and Modelling of Earthquakes, Volcanoes and Tectonics, a partnership between UK Universities and the British Geological Survey. AB, TJC and SR were also partly supported by the Leverhulme Trust through Research Grant RPG-2021-336. Much of this work was undertaken on ARC4, part of the High Performance Computing facilities at the University of Leeds, UK and using the ObsPy seismology toolbox for Python (M. Beyreuther *et al.* 2010).

The ISC (TG and RG) is supported by 80 Member-Institutions in 50 countries (www.isc.ac.uk/members/ last access: June 2025), including the National Science Foundation award EAR 2414178 and the Royal Society award INT004. The ISC is also grateful to the following organizations that help to fund the ISC development projects: CTBTO, FM Global, the Lighthill Risk Network, AXA XL, USGS, SARA, GeoSIG, GaiaCode and MS&AD.

We thank Doug Wiens and an anonymous reviewers for their useful comments on this paper.

SUPPORTING INFORMATION

Supplementary data are available at *GJIRAS* online.

Janin_et_al_2026_GJI_SuppMat.zip

Please note: Oxford University Press is not responsible for the content or functionality of any supporting materials supplied by the authors. Any queries (other than missing material) should be directed to the corresponding author for the paper.

DATA AVAILABILITY

All seismic data used in this study are openly available from BGR at http://eida.bgr.de, ETH at http://eida.ethz.ch, GEONET at http://service.geonet.org.nz, GFZ at http://geofon.gfz⟨plxhyp⟩PLXHYP⟨/plxhyp⟩potsdam.de, ICGC at http://ws.icgc.cat, INGV at http://webservices.ingv.it, IPGP at http://ws.ipgp.fr, IRIS at http://service.iris.edu, KNMI at http://rdsa.knmi.nl, LMU at http://erde.geophysik.uni⟨plxhyp⟩PLXHYP⟨/plxhyp⟩muenchen.de, NIEP at http://eida⟨plxhyp⟩PLXHYP⟨/plxhyp⟩sc3.infp.ro, NOA at http://eida.gein.noa.gr, ORFEUS at http://www.orfeus⟨plxhyp⟩PLXHYP⟨/plxhyp⟩eu.org, RESIF at http://ws.resif.fr, SCEDC at http://service.scedc.caltech.edu, TEXNET at http://rtserve.beg.utexas.edu, UIB-NORSAR at http://eida.geo.uib.no, and USP at http://sismo.iag.usp.br. A full list of seismic networks used, and their DOIs, is provided in supplementary material. Final earthquake catalogues for the South American Subduction Zone are provided in supplementary material.

The code is available at https://github.com/AliceBlackwell/Depth_Phase_Array_Analysis.

REFERENCES

Abers, G., Nakajima, J., van Keken, P., Kita, S. & Hacker, B., 2013. Thermal-petrological controls on the location of earthquakes within subducting plates, *Earth planet. Sci. Lett.*, **369–370,** 178–187.

Benioff, H., 1949. Seismic evidence for the fault origin of oceanic deeps, *Bull. Geol. Soc. Am.*, **60**(12), 1837–1856.

Beyreuther, M., Barsch, R., Krischer, L., Megies, T., Behr, Y. & Wassermann, J., 2010. ObsPy: A python toolbox for seismology, *Seismol. Res. Lett.,* **81**(3), 530–533.

Bilek, S., 2010. Invited review paper: Seismicity along the South American subduction zone: Review of large earthquakes, tsunamis, and subduction zone complexity, *Tectonophysics,* **495**(1-2), 2–14.

Blackwell, A., Craig, T. & Rost, S., 2024. Automatic relocation of intermediate-depth earthquakes using adaptive teleseismic arrays, *Geophys. J. Int.,* **239**(2), 821–840.

Bondár, I. & Storchak, D., 2011. Improved location procedures at the International Seismological Centre, *Geophys. J. Int.,* **186**(3), 1220–1244.

Brudzinski, M., Thurber, C., Hacker, B. & Engdahl, E., 2007. Global prevalence of double Benioff zones, *Science,* **316**(5830), 1472–1474.

Craig, T., 2019. Accurate depth determination for moderate-magnitude earthquakes using global teleseismic data, *J. geophys. Res.: Solid Earth,* **124**(2), 1759–1780.

Craig, T., Methley, P. & Sandiford, D., 2022. Imbalanced moment release within subducting plates during initial bending and unbending, *J. geophys. Res.: Solid Earth,* **127**(3), e2021JB023658.

Crotwell, H., Owens, T. & Ritsema, J., 1999. The TauP Toolkit: Flexible seismic travel-time and ray-path utilities, *Seismol. Res. Lett.,* **70,** 154–160.

Delouis, B. & Legrand, D., 2007. Mw 7.8 Tarapaca intermediate depth earthquake of 13 June 2005 (northern Chile): Fault plane identification and slip distribution by waveform inversion, *Geophys. Res. Lett.,* **34**(1), 1–6.

Dziewonski, A., Chou, T. & Woodhouse, J., 1981. Determination of earthquake source parameters from waveform data for studies of global and regional seismicity., *J. geophys. Res.,* **86**(B4), 2825–2852.

Ekström, G., Nettles, M. & Dziewoński, A., 2012. The global CMT project 2004-2010: Centroid-moment tensors for 13,017 earthquakes, *Phys. Earth planet. Inter.,* **200–201,** 1–9.

Engdahl, E., van der Hilst, R. & Buland, R., 1998. Global teleseismic earthquake relocation with improved travel times and procedures for depth determination, *Bull. seism. Soc. Am.,* **88**(3), 722–743.

Espurt, N., Funiciello, F., Martinod, J., Guillaume, B., Regard, V., Faccenna, C. & Brusset, S., 2008. Flat subduction dynamics and deformation of the South American plate: Insights from analog modeling, *Tectonics,* **27**(3), 1–19.

Ester, M., Kriegel, H., Sander, J. & Xu, X., 1996. A density-based algorithm for discovering clusters a density-based algorithm for discovering clusters in large spatial databases with noise, in *Proceedings - 2nd International Conference on Knowledge Discovery and Data Mining, KDD 1996,* pp. 226–231, eds Simoudis, E., Han, J. & Fayyad, U., AAAI Press, Portland, Oregon.

Flament, N., Gurnis, M., Müller, R., Bower, D. & Husson, L., 2015. Influence of subduction history on South American topography, *Earth planet. Sci. Lett.,* **430,** 9–18.

Florez, M. & Prieto, G., 2017. Precise relative earthquake depth determination using array processing techniques, *J. geophys. Res.: Solid Earth,* **122**(6), 4559–4571.

Florez, M. & Prieto, G., 2019. Controlling Factors of Seismicity and Geometry in Double Seismic Zones, *Geophys. Res. Lett.,* **46**(8), 4174–4181.

Gao, Y., Yuan, X., Heit, B., Tilmann, F., van Herwaarden, D., Thrastarson, S., Fichtner, A. & Schurr, B., 2021. Impact of the Juan Fernandez Ridge on the Pampean Flat Subduction Inferred From Full Waveform Inversion, *Geophys. Res. Lett.,* **48**(21), e2021GL095509.

Global Volcanism Program, S.I., 2024. *VE. Venzkeolcanoes of the World, v. 5.2.7.*

Hayes, G., 2017. The finite, kinematic rupture properties of great-sized earthquakes since 1990, *Earth planet. Sci. Lett.,* **468,** 94–100.

Hayes, G., Wald, D. & Johnson, R., 2012. Slab1.0: A three-dimensional model of global subduction zone geometries, *J. geophys. Res.: Solid Earth,* **117**(1), 1–15.

Hayes, G., Moore, G., Portner, D., Hearne, M., Flamme, H., Furtney, M. & Smoczyk, G., 2018. Slab2, a comprehensive subduction zone geometry model, *Science,* **362**(6410), 58–61.

Hosseini, K. & Sigloch, K., 2017. ObspyDMT: A Python toolbox for retrieving and processing large seismological data sets, *Solid Earth,* **8**(5), 1047–1070.

Hu, Y., Yagi, Y., Okuwaki, E. & Shimizu, K., 2021. Back-propagating rupture evolution within a curved slab during the 2019 M_w8.0 Peru intraslab earthquake, *Geophys. J. Int.,* **227**(3), 1602–1611.

International Seismological Centre, 2024. On-line Bulletin, https://doi.org/10.31905/D808B830.

Kennett, B., Engdahl, E. & Buland, R., 1995. Constraints on seismic velocities in the Earth from traveltimes, *Geophys. J. Int.,* **122**(1), 108–124.

Kuge, K., Kase, Y., Urata, Y., Campos, J. & Perez, A., 2010. Rupture characteristics of the 2005 Tarapaca, northern Chile, intermediate-depth earthquake: Evidence for heterogeneous fluid distribution across the subducting oceanic plate?, *J. geophys. Res.: Solid Earth,* **115**(9), 1–15.

Liu, W. & Yao, H., 2020. Rupture Process of the 26 May 2019 Mw 8.0 Northern Peru Intermediate-Depth Earthquake and Insights Into Its Mechanism, *Geophys. Res. Lett.,* **47**(4).

Luo, H., Zeng, H., Shi, Q., Wang, T., Liao, M., Hu, J. & Wei, S., 2023. Could thermal pressurization have induced the frequency-dependent rupture during the 2019 M_w8. 0 Peru intermediate-depth earthquake?, *Geophys. J. Int.,* **232**(1), 115–127.

Münchmeyer, J., Saul, J. & Tilmann, F., 2024. Learning the deep and the shallow: deep-learning-based depth phase picking and earthquake depth estimation, *Seismol. Res. Lett.,* **95**(3), 1543–1557.

Pedregosa, F. *et al.*, 2011. Scikit-learn: Machine Learning in Python Gaël Varoquaux Bertrand Thirion Vincent Dubourg Alexandre Passos PEDREGOSA, VAROQUAUX, GRAMFORT ET AL. Matthieu Perrot, *J. Mach. Learn. Res.,* **12,** 2825–2830.

Peyrat, S. *et al.*, 2006. Tarapacá intermediate-depth earthquake (M_w 7.7, 2005, northern Chile): A slab-pull event with horizontal fault plane constrained from seismologic and geodetic observations, *Geophys. Res. Lett.,* **33**(22), 1–6.

Portner, D. & Hayes, G., 2018. Incorporating teleseismic tomography data into models of upper mantle slab geometry, *Geophys. J. Int.,* **215**(1), 325–332.

Rodríguez, E. *et al.*, 2024. Seismic imaging of the Northern Andean subduction zone from teleseismic tomography: a torn and fragmented Nazca slab, *Geophys. J. Int.,* **236**(1), 593–606.

Rost, S. & Thomas, C., 2002. Array seismology: Methods and applications, *Rev. Geophys.,* **40**(3), 2–1.

Sandiford, D., Moresi, L., Sandiford, M., Farrington, R. & Yang, T., 2020. The fingerprints of flexure in slab seismicity, *Tectonics,* **39**(8).

Schimmel, M. & Paulssen, H., 1997. Noise reduction and detection of weak, coherent signals through phase-weighted stacks, *Geophys. J. Int.,* **130**(2), 497–505.

Sippl, C., Schurr, B., Asch, G. & Kummerow, J., 2018. Seismicity structure of the Northern Chile forearc from >100 000 double-difference relocated hypocenters, *J. geophys. Res.: Solid Earth,* **123**(5), 4063–4087.

Sippl, C., Dielforder, A., John, T. & Schmalholz, S.M., 2022. Global constraints on intermediate-depth intraslab stresses from slab geometries and mechanisms of double seismic zone earthquakes, *Geochem. Geophys. Geosyst.,* **23**(9), e2022GC010498. doi: 10.1029/2022GC010498.

Sippl, C., Schurr, B., Münchmeyer, J., Barrientos, S. & Oncken, O., 2023. The Northern Chile forearc constrained by 15 years of permanent seismic monitoring, *J. South Am. Earth Sci.,* **126**(March), 104326.

Trenkamp, R., Kellogg, J., Freymueller, J. & Mora, H., 2002. Wide plate margin deformation, southern Central America and northwestern South America, CASA GPS observations, *J. South Am. Earth Sci.,* **15**(2), 157–171.

Vallée, M. *et al.*, 2023. Self-reactivated rupture during the 2019 M_w = 8 Northern Peru Intraslab earthquake, *Earth planet. Sci. Lett.,* **601,** 117886. doi: 10.1016/j.epsl.2022.117886.

Wadati, K., 1935. On the activity of deep-focus earthquakes in the Japan Islands and neighborhoods, *Geophys. Magaz.,* **8,** 305–325.

Wagner, L. & Okal, E., 2019. The Pucallpa Nest and its constraints on the geometry of the Peruvian Flat Slab, *Tectonophysics,* **762**(October 2018), 97–108.

Wang, K., 2002. Unbending combined with dehydration embrittlement as a cause for double and triple seismic zones, *Geophys. Res. Lett.,* **29**(18), 1889.

Ward, J., Thorne, M., Nowacki, A. & Rost, S., 2023. Upper mantle structure beneath the contiguous US resolved with array observations of SKS multipathing and slowness vector perturbations, *J. geophys. Res.: Solid Earth,* **128**(7), e2022JB026260.

Wimpenny, S., Craig, T. & Marcou, S., 2023. Re-examining temporal variations 966 in intermediate-depth seismicity, *J. geophys. Res.: Solid Earth,* **128**(6), e2022JB026269.

Ye, L., Lay, T. & Kanamori, H., 2020. Anomalously low aftershock productivity of the 2019 M_W 8.0 energetic intermediate-depth faulting beneath Peru, *Earth planet. Sci. Lett.,* **549**. doi: 10.1016/j.epsl.2020.116528.

Zandt, G., Velasco, A. & Beck, S., 1994. Composition and thickness of the southern Altiplano crust, Bolivia, *Geology,* **22**(11), 1003–1006.

Zeng, L., Ye, L., Yao, H., Liu, W., Si, D., Lay, T. & Yang, T., 2025. Narrow intermediate-depth seismogenic band related to flexural strain in relatively dry Peruvian flat slab, *Commun. Earth Environ.,* **6**(1), 1–14.